JACS
JOURNAL OF THE AMERICAN CHEMICAL SOCIETY
pubs.acs.org/JACS
Article

Kinetic Modulation of Carbon Nanotube Growth in Direct Spinning for High-Strength Carbon Nanotube Fibers

Zuncheng Hu,[⊥] Xiucai Sun,[⊥] Xinshi Zhang, Xiangzheng Jia, Xueting Feng, Mingwei Cui, Enlai Gao, Liu Qian,* Xin Gao,* and Jin Zhang*

Cite This: https://doi.org/10.1021/jacs.4c01705

Read Online

ACCESS | Metrics & More | Article Recommendations | Supporting Information

ABSTRACT: With impressive individual properties, carbon nanotubes (CNTs) show great potential in constructing high-performance fibers. However, the tensile strength of as-prepared carbon nanotube fibers (CNTFs) by floating catalyst chemical vapor deposition (FCCVD) is plagued by the weak intertube interaction between the essential CNTs. Here, we developed a chlorine (Cl)/water (H_2O)-assisted length furtherance FCCVD (CALF-FCCVD) method to modulate the intertube interaction of CNTs and enhance the mechanical strength of macroscopic fibers. The CNTs acquired by the CALF-FCCVD method show an improvement of 731% in length compared to that by the conventional iron-based FCCVD system. Moreover, CNTFs prepared by CALF-FCCVD spinning exhibit a high tensile strength of 5.27 ± 0.27 GPa (4.62 ± 0.24 N/tex) and reach up to 5.61 GPa (4.92 N/tex), which outperforms most previously reported results. Experimental measurements and density functional theory calculations show that Cl and H_2O play a crucial role in the furtherance of CNT growth. Cl released from the decomposition of methylene dichloride greatly accelerates the growth of the CNTs; H_2O can remove amorphous carbon on the floating catalysts to extend their lifetime, which further modulates the growth kinetics and improves the purity of the as-prepared fibers. Our design of the CALF-FCCVD platform offers a powerful way to tune CNT growth kinetics in direct spinning toward high-strength CNTFs.

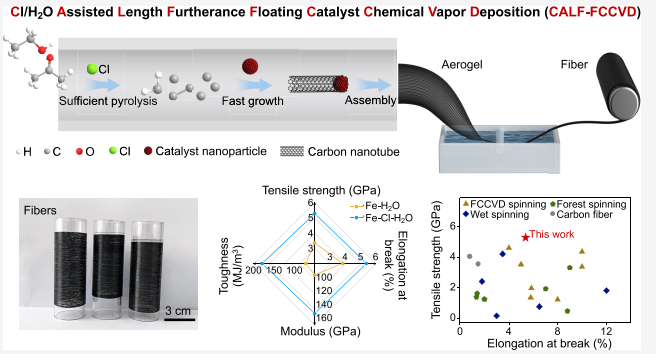

INTRODUCTION

Carbon nanotubes (CNTs) have received widespread attention from researchers since they were observed in 1991.[1] Along the tube axis, the strong covalent C−C bonds endow CNTs with an ultrahigh elastic modulus (up to 1 TPa)[2] and tensile strength (up to 100 GPa).[3] Benefiting from the unique structure and ultrahigh intrinsic properties, CNTs have been widely considered as an ideal building block to construct fibers with high strength and toughness, which are expected to surpass carbon fibers.[4] There are three main types of preparation methods of carbon nanotube fibers (CNTFs): wet spinning,[5] forest spinning,[6] and floating catalyst chemical vapor deposition (FCCVD) spinning.[7]

Among them, FCCVD can realize continuous production of CNTFs directly after CNT growth and has the potential for large-scale CNTF preparation. In the FCCVD system, the residence time of catalysts in the high-temperature zone is very short (often a few seconds to tens of seconds), and the catalyst is easily poisoned by amorphous carbon coating, which limits the length of CNTs in terms of growth time. Besides, the growth kinetics of CNTs is greatly influenced by the supply rate of active carbon species such as carbon atoms (C)[8] and carbon dimers (C_2),[9] which also determines the length of CNTs in terms of growth rate. Three-level hierarchical model[10] shows the effect of the length of individual CNTs on the mechanical properties of CNTFs. On the one hand, the failure probability of CNTs rises as the length of CNTs increases due to the presence of more defects within longer CNTs. On the other hand, the overlap area between the adjacent CNTs becomes larger with the increasing length of CNTs, which results in enhanced interaction and sufficient load transfer between CNTs. The load transfer plays a leading role in mechanical performance, according to the theoretical model. Therefore, increasing the length of the CNTs in the as-spun CNTFs is an effective way to improve the fiber strength. In addition, although the mechanical properties of CNTFs have been further improved by optimizing spinning and postprocessing technologies on the CNTF level (or CNT bundle level), including adjusting winding rates,[11] solvent

Received: February 4, 2024
Revised: March 30, 2024
Accepted: April 1, 2024

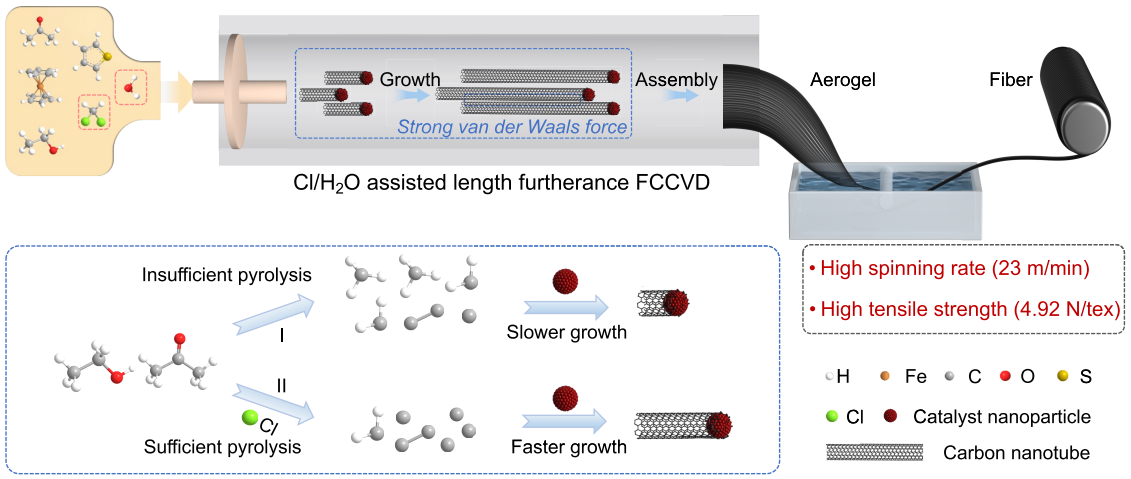

Figure 1. Schematic of high-strength CNTF preparation by the CALF-FCCVD method. Cl/H_2O assisted length furtherance floating catalyst chemical vapor deposition (CALF-FCCVD) process to fast grow long CNTs. A large number of as-prepared CNTs assemble together to obtain high-strength CNTFs. Cl released from CH_2Cl_2 pyrolysis is beneficial for the sufficient pyrolysis of carbon sources, generating more active carbon species (C or C_2) for the growth of CNTs, thereby increasing the growth rate of CNTs. Introducing H_2O avoids the poisoning of catalyst nanoparticles by amorphous carbon, extending the lifetime of the catalysts and increasing the growth time of CNTs.

densification,[12] rolling densification,[13] acid treatment,[14,15] and particle beam irradiation,[16] the tensile strength (<5 GPa) of CNTFs by the FCCVD spinning to date has been far below expected due to the friction and slippage between as-grown short CNTs.[17,18] The length modulation of CNTs in the as-spun CNTFs is the premise for achieving excellent performance. However, studies on the modulation of CNTs in direct spinning are still in their infancy.

Herein, we developed a chlorine (Cl)/ water (H_2O)-assisted length furtherance FCCVD (termed CALF-FCCVD) method to modulate the length of the CNTs and enhance the mechanical strength of macroscopic fibers (Figure 1). Cl released from methylene dichloride (CH_2Cl_2) pyrolysis was introduced into the growth zone to assist the carbon source cracking, generating more C or C_2 species for the growth of CNTs, thus increasing the growth rate of CNTs. A certain amount of H_2O was added to avoid the poisoning of catalyst nanoparticles by amorphous carbon, extending the lifetime of the catalysts and increasing the growth time of the CNTs. By the CALF-FCCVD method, the strength of the as-spun CNTFs reached 1.77 GPa. After chlorosulfonic acid (CSA) stretching and rolling process to increase the orientation and packing density of the CNTFs, their strength reached 5.61 GPa (4.92 N/tex). This work clearly shows that regulating the growth kinetics of CNTs is an important way to prepare high-strength CNTFs.

RESULTS AND DISCUSSION

High-Performance As-Spun CNTFs by the CALF-FCCVD Method. Modulating the composition of the reaction solution is crucial for the continuous collection of high-performance fibers. We performed a modified FCCVD method to directly synthesize high-strength CNTFs (Figure 1) by adding the Cl/H_2O contained precursors. CH_2Cl_2 and H_2O were simultaneously introduced into the precursor solution for the length modulation of CNTs, for the first time. Cl released from the decomposition of CH_2Cl_2 accelerated the pyrolysis of carbon sources and lengthened the growth of as-grown CNTs. H_2O can remove the amorphous carbon covered on the catalyst surface[19] and reduce the weak junction formed by amorphous carbon to improve the spinning continuity.[20] The precursor solution consisting of acetone and ethanol with dissolved ferrocene and thiophene, which acted as carbon sources and catalysts, was injected into the reactor at a rate of 30 mL/h. The reactor furnace was set at 1300 °C and 3000 standard cubic centimeters per minute (sccm) hydrogen, and 2000 sccm argon gas was introduced into the furnace tube. The reactants collide randomly with the gas flow, and CNTs were formed in the high-temperature zone. The as-grown CNTs were assembled into aerogels and were immersed in water for densification to obtain as-spun CNTFs. The molar ratio of Fe to H_2O in the precursor solution was 1:207 for a high-speed continuous spinning. Further, the molar ratio of Fe/Cl was optimized to improve the fiber strength.

Figure 2a and Supplementary Figure 1 show the strength of the as-spun fibers using the CALF-FCCVD method. The CNTFs prepared by the conventional FCCVD method (without Cl-contained precursor) were chosen as the control. The correlation between the strength of CNTFs and the Fe−Cl ratio showed a nonlinear relation. As the Cl content increased, the strength of CNTFs increased and then decreased. The CNTFs of Fe−Cl−H_2O (1:1.6:207) showed the highest strength of 1.77 ± 0.02 GPa, which is a 33% increase in strength compared with the fibers prepared by the conventional FCCVD method (1.33 ± 0.09 GPa).

The inset in Figure 2a shows a digital photograph of the as-spun CNTFs (hundreds of meters) prepared by the CALF-FCCVD method at a high spinning speed of 23 m/min (Supplementary Movie 1). The as-spun CNTFs of Fe−Cl−H_2O (1:1.6:207) exhibit a clean surface with the CNTs tightly intertwining together (Figure 2b,c). The cross-sectional transmission electron microscope (TEM) image shows the fiber consisted of multiwalled CNTs with an average diameter of 9.93 nm (Figure 2d and Supplementary Figure 2). The introduction of Cl did not affect the diameter of the CNTs (Supplementary Figure 2). Figure 2e shows the typical multiwalled CNT connected to a catalyst nanoparticle in the fiber. A high-resolution TEM image of the nanoparticle is shown in Figure 2f (red frame in Supplementary Figure 3). The lattice distance is 0.210 nm, corresponding to the (2 1 1)

https://doi.org/10.1021/jacs.4c01705
J. Am. Chem. Soc. XXXX, XXX, XXX−XXX

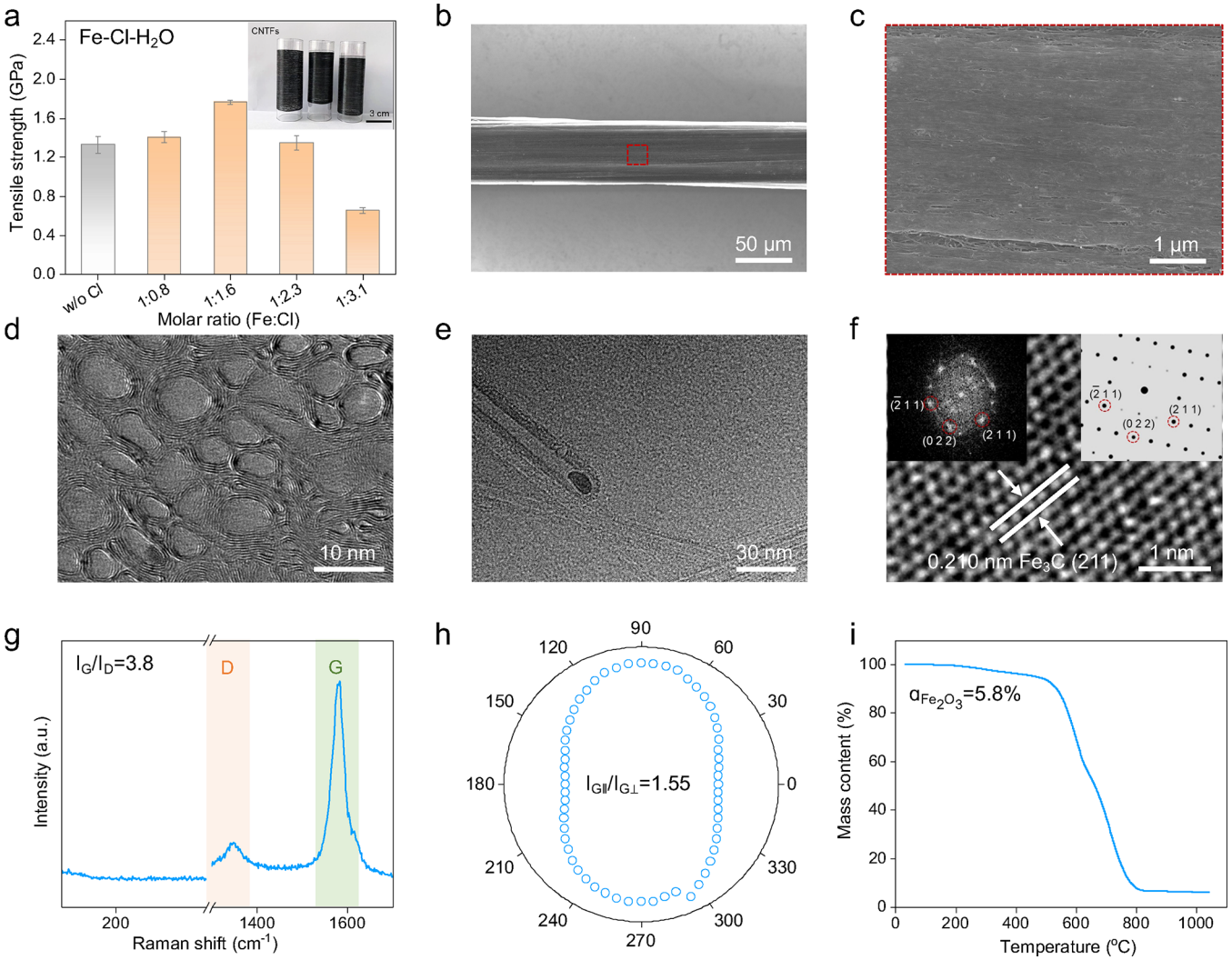

Figure 2. Structure and properties of as-spun CNTFs by the CALF-FCCVD method.(a) On the basis of Fe−H_2O (1:207), the comparison of strength of CNTFs with different contents of Cl. Each bar stands for the mean of replicated tensile strength measurements. Number of replicated measurements (n) is as follows: Fe−H_2O (1:207) (n = 5), Fe−Cl−H_2O (1:0.8:207) (n = 4), Fe−Cl−H_2O (1:1.6:207) (n = 5), Fe−Cl−H_2O (1:2.3:207) (n = 5), and Fe−Cl−H_2O (1:3.1:207) (n = 4). The inset is a digital photograph of CNTFs. (b) Scanning electron microscope (SEM) image of CNTFs obtained under Fe−Cl−H_2O (1:1.6:207). (c) Zoom-in image of the red frame in panel (b). (d) Cross-sectional TEM image of the CNTFs. (e) TEM image of a CNT connected to a catalyst nanoparticle. (f) High-resolution TEM image of the nanoparticle. Inset: the left panel is the corresponding FFT pattern; the right panel is the simulated diffraction pattern of Fe_3C along the zone axis of [0−1 1]. (g) Raman spectrum, (h) polarized Raman spectrum, and (i) TGA of the CNTFs were obtained under Fe−Cl−H_2O (1:1.6:207).

facet of the iron carbide (Fe_3C) phase.[21] The fast Fourier transform (FFT) pattern (inset of Figure 2f) agrees perfectly with the simulated diffraction pattern of Fe_3C along the zone axis of [0−1 1].

Figure 2g presents the ratio of the intensity of the G band to that of the D band (I_G/I_D) in the Raman spectra. The D band is related to topological defects and disorders in carbonaceous materials while the G band corresponds to the graphitized carbon. Higher I_G/I_D values indicate a higher quality of CNTs. The CNTFs of Fe−Cl−H_2O (1:1.6:207) show the highest I_G/I_D of 3.8 among all the conditions (Supplementary Figure 4). Cl in the gas phase is beneficial for carbon source cracking. The introduction of an appropriate amount of Cl reduced the amorphous carbon formation. However, excessive Cl will generate excessive carbon species, thus increasing the content of amorphous carbon. Linear density is one of the important physical and geometric characteristics of fibers and describes the thickness of fibers. The linear density of CNTFs increased with the increase of Cl content (Supplementary Figure 5), further demonstrating that Cl can assist in the cracking of carbon sources. The energy-dispersive X-ray spectroscopy (EDS) shows no signal of Cl in the as-spun fibers (Supplementary Figure 6), which indicates that Cl does not dope the CNTFs.

To characterize the fiber orientation, we used polarized Raman spectroscopy for quantitative analysis.[15,22] The ratio of the intensity of the G band of the Raman spectrum for the polarization parallel to the fiber axis to that for the polarization perpendicular to the fiber axis ($I_{G\parallel}/I_{G\perp}$) can characterize the orientation of as-prepared fibers. The higher $I_{G\parallel}/I_{G\perp}$ means that the fiber has a higher orientation degree along the axial direction. The CNTFs obtained under Fe−Cl−H_2O (1:1.6:207) show that the $I_{G\parallel}/I_{G\perp}$value is 1.55 (Figure 2h), which is lower than that ($I_{G\parallel}/I_{G\perp}$ = 1.85, Supplementary Figure 7) of Fe−H_2O (1:207). The longer CNTs are easier to entangle together, resulting in a decrease in the orientation

https://doi.org/10.1021/jacs.4c01705
J. Am. Chem. Soc. XXXX, XXX, XXX−XXX

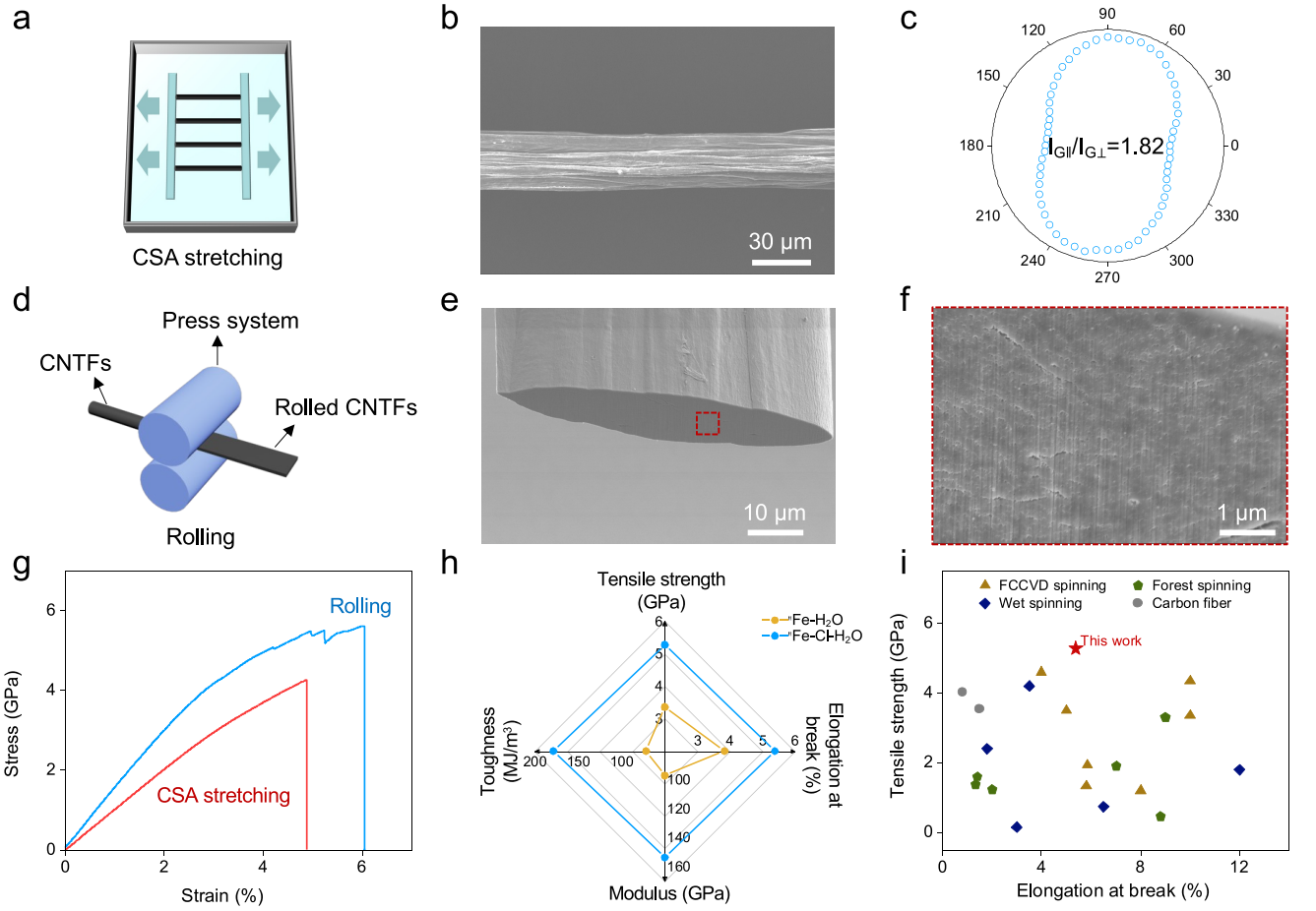

Figure 3. Mechanical properties of CNTFs after post-treatment.(a) Schematic of CSA stretching. (b) SEM image and (c) polarized Raman spectrum of the CNTFs obtained under Fe−Cl−H_2O (1:1.6:207) after CSA stretching. (d) Schematic of rolling. (e) Cross-sectional SEM image of the CNTFs obtained under Fe−Cl−H_2O (1:1.6:207) after rolling. (f) Enlarged image of CNTFs (red frame in panel (e)). (g) Stress−strain curves of CNTFs after CSA stretching and rolling. (h) Comparison of the mechanical properties of CNTFs obtained under Fe−H_2O (1:207) and Fe−Cl−H_2O (1:1.6:207). (i) Comparison of tensile strength and elongation at break of our CNTFs with commercial carbon fibers[24] and the CNTFs prepared by FCCVD spinning,[7,11,13,25−28] forest spinning,[29−34] and wet spinning.[5,35−38] The exact mechanical performance data for different methods are summarized in Supplementary Tables 1 and 2.

degree. Thermogravimetric analysis (TGA) shows the content of residual Fe_2O_3 in the fiber is as low as 5.8% (Figure 2i). Assuming all catalysts are oxidized to Fe_2O_3, the residual Fe content is 4.1% (Supplementary Figure 8b).

Post-Treatment of As-Spun CNTFs. To further improve the mechanical properties of as-spun CNTFs, we densified and aligned the internal structures of CNTFs using CSA stretching and rolling densification. The CSA is known as a thermodynamic solvent for CNT dissolution.[23] Therefore, we first performed CSA stretching (Figure 3a) on the as-spun CNTFs using the optimal conditions of Fe−Cl−H_2O (1:1.6:207), with a stretching ratio of 5%. Figure 3b shows the surface morphology of the fiber after stretching. The orientation factor ($I_{G\parallel}/I_{G\perp}$) increases from 1.55 to 1.82 (Figure 3c and Supplementary Figure 9c). In addition, the proportion of voids in the cross-section is significantly reduced and the packing density of the fiber is also improved (Supplementary Figure 10d). Benefiting from the improvement of orientation and packing density, the tensile strength of the fiber was improved to 3.88 ± 0.29 GPa, with a maximum of 4.26 GPa (Figure 3g and Supplementary Figure 11b). Moreover, we performed a rolling densification treatment (Figure 3d) to further compact the CNTFs. The fiber shows a narrow band shape after rolling (Figure 3e). Cross-sectional SEM images indicate that CNTs are tightly packed in the fiber (Figure 3f). After rolling, the mechanical performance was greatly improved compared to the as-spun CNTFs. The tensile strength of the processed fibers is 5.27 ± 0.27 GPa (Figure 3g and Supplementary Figure 11d), with a modulus of 153.69 ± 13.86 GPa, a toughness of 178.44 ± 30.31 MJ/m^3, and an elongation at break of 5.38 ± 0.56%, displaying 57, 59, 150, and 40% increases compared to CNTFs obtained via the conventional FCCVD method (without Cl precursor) after post-treatment (Figure 3h). The mechanical performances of as-prepared fibers using the CALF-FCCVD method outperform most previously reported CNTFs (Figure 3i).

Mechanism for Cl/H_2O-Assisted High-Strength CNTF Preparation. We have developed a three-level hierarchical model[10] to understand the mechanical behavior of CNTFs, which can be used to explain the performance improvement of CNTFs in this work. The introduction of Cl/H_2O increases the length of CNTs by 70−150% compared with the conventional FCCVD method (see Experimental Section in the Supporting Information for details). This length increase promotes the load transfer efficiency, which helps to improve the mechanical strength of the fibers. However, it should be

https://doi.org/10.1021/jacs.4c01705
J. Am. Chem. Soc. XXXX, XXX, XXX−XXX

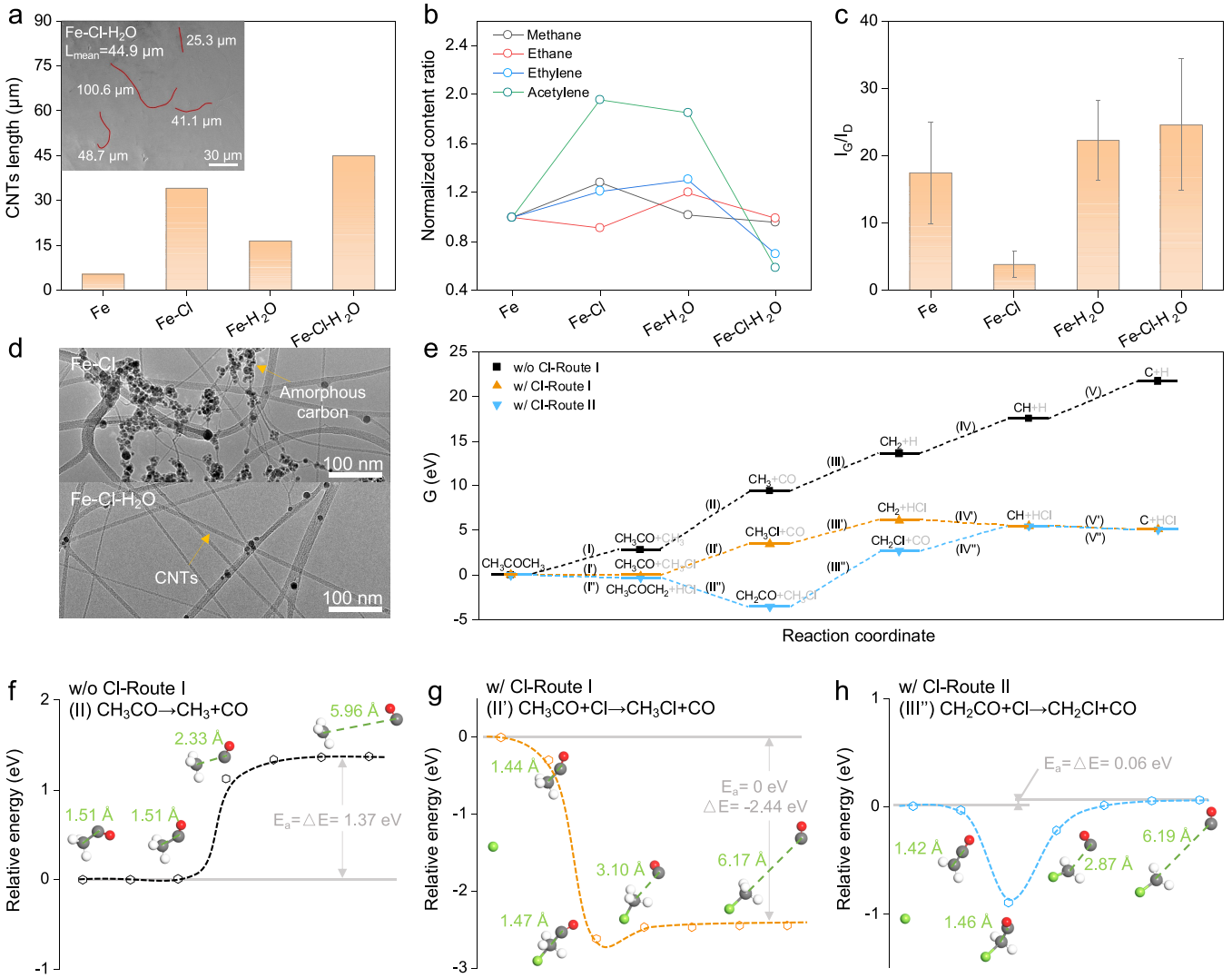

Figure 4. Mechanism analysis for Cl/H_2O-modulated CNT growth.(a) Average CNTs length under different growth conditions. Inset is a typical SEM image of CNTs. The molar ratio of Fe to Cl is 1:2; the molar ratio of Fe to H_2O is 1:2; the molar ratio of Fe to Cl to H_2O is 1:2:2. (b) Normalized contents of CH_4, C_2H_6, C_2H_4, and C_2H_2 in reaction exhaust under different conditions measured by GC−MS. The relative concentration of carbon-containing gas of the reaction exhaust gas indicates the usage of the carbon sources. All values are normalized to those of Fe. (c) I_G/I_D of CNTs under different growth conditions. The number of replicates for each experimental condition is 5. (d) TEM images of as-grown CNTs. (e) Calculated free energy of acetone decomposition with and without Cl. Energy profile of the rate-limiting step in (f) Route I without Cl introduction, (g) Route I with Cl introduction, and (h) Route II with Cl introduction. Compared to the acetone decomposition without Cl introduction, the Cl-modulated reactions have lower ΔG and activation energy (E_a); both factors lead to an elevated concentration of reactive carbon species (C or C_2) and, consequently, fast CNT growth. The green numbers represent the distance between two carbon atoms connected by green dashed line. Green, red, gray, and white spheres are chlorine, oxygen, carbon, and hydrogen atoms, respectively.

noted that accurate characterization of the length of CNTs in these macroscopic CNTFs is challenging due to the entanglement among CNTs.

To visualize the mechanism for Cl/H_2O-assisted long CNTs growth toward high-strength CNTF preparation, we used the horizontal furnace to prepare a small amount of CNTs by the CALF-FCCVD method. The furnace temperature was set at 1100 °C, the injection rate of the catalyst solution was 10 μL/min, and the total flow rate of argon and hydrogen was 1000 sccm. The conventional FCCVD method without Cl/H_2O precursors was performed for comparison. Four different reaction conditions with different carbon source concentrations (C1−C4, see Experimental Section in the Supporting Information for details) were conducted for CNT growth. The length of as-grown CNTs can be fitted by statistical distribution and meet the log-normal distribution (Supplementary Figures 12−16). Without Cl and H_2O addition (denoted as Fe; control group), the as-grown CNTs are shorter with length of 5.4 ± 3.2 μm (Supplementary Figure 12). When H_2O was introduced into the precursor solution, the as-grown CNTs became longer and their length increased to 16.6 ± 13.6 μm (Supplementary Figures 15 and 17b), with an average diameter of 1.89 nm (Supplementary Figure 18). Further, we added CH_2Cl_2 to the reaction precursor solutions. The molar ratio of Fe to Cl to H_2O is 1:2:2. CH_2Cl_2 will generate Cl through pyrolysis,[39] which can regulate the gas-phase reaction, facilitating the dehydrogenation process of hydrocarbons.[40] The length of as-grown CNTs is 44.9 ± 29.3 μm (Figure 4a and Supplementary Figure 16b), which shows a

https://doi.org/10.1021/jacs.4c01705
J. Am. Chem. Soc. XXXX, XXX, XXX−XXX

731% increase in length compared with that of the control group (5.4 ± 3.2 μm).

Gas chromatography−mass spectrometry (GC−MS), Raman spectroscopy, and TEM were performed to understand the growth process of CNTs. The carbon-containing gases in the reaction exhaust of conventional Fe catalytic growth system are methane, ethane, ethylene, and acetylene (Supplementary Figure 19 and Supplementary Table 3). With the addition of H_2O, both the concentration of some carbon-containing gases (methane, ethane, ethylene, and acetylene) and the value of I_G/I_D for the as-grown CNTs increased (Figure 4b,c and Supplementary Figures 20 and 21c), which indicated that the increase in CNTs length mainly resulted from the extended catalyst life.[41] When Cl was introduced into the system, the ethane content decreased, while the others increased compared to the control group. Moreover, the I_G/I_D ratio of as-grown CNTs is lower compared with the control group (Figure 4c and Supplementary Figures 20 and 22c). The quality (I_G/I_D) of the product decreases with the increase of Cl content (Supplementary Figure 23). When the Cl content is higher than the threshold (Fe:Cl = 1:8), the product is mainly amorphous carbon (Supplementary Figure 24). Therefore, although the length of CNTs increased after Cl addition, some catalysts were still coated by amorphous carbon and deactivated (Figure 4d). The X-ray photoelectron spectroscopy (XPS) spectrum shows that the CNTs are free of Cl element (Supplementary Figure 25), which implies that Cl works during the growth process. When Cl and H_2O were introduced into the FCCVD system simultaneously, the concentration of some carbon-containing gases (methane, ethane, ethylene, and acetylene) decreased, while the I_G/I_D ratio increased compared with the control group (Figure 4b,c and Supplementary Figures 20 and 26c). The TEM images (Figure 4d) show that the addition of Cl and H_2O leads to less amorphous carbon deposition and improves the purity of the CNTs. Therefore, Cl/H_2O plays a crucial role in tuning the growth kinetics of CNTs.

To attain an in-depth understanding of the effect of Cl on CNT growth kinetics, we carried out density functional theory (DFT) calculations to simulate the carbon source (acetone and ethanol) decomposition process. According to the overlap populations of chemical bonds (Supplementary Figure 27a), the C−C bond in acetone has the smallest overlap population and the weakest strength, which causes it to break more frequently during gas phase pyrolysis. Subsequently, the hydrocarbon species continue to dehydrogenate in the high-temperature gas phase to provide precursor for the growth of CNTs (following Route I: $CH_3COCH_3 \rightarrow CH_3CO + CH_3 \rightarrow CH_3 + CO \rightarrow CH_{3-x} + xH$), which is consistent with the results of this route (Route I) as the main pathway in the literature[42] (Supplementary Figure 28). Therefore, we first take the gradual pyrolysis of acetone in Route I as the research object and preliminarily evaluate the influence of Cl through the thermodynamic energy changes of Gibbs free energy (G).

Thermodynamic analysis (Figure 4e and Supplementary Table 4) reveals that the energy gain of gradual pyrolysis of acetone to carbon atoms following Route I is significant, and each acetone molecule needs to absorb 21.70 eV of energy to achieve complete decomposition. Among them, the second step, $CH_3CO \rightarrow CH_3$+CO, has the largest free energy increment (ΔG, 6.59 eV), thus serving as a speed limiting step to limit the acetone pyrolysis process. When Cl is introduced into the gas phase, active Cl atoms collide with acetone molecules to create a connection, which weakens the C−C bonds due to electron relaxation, resulting in the overall ΔG dramatically reduced to 5.11 eV during the full pyrolysis of acetone into carbon atoms. Therefore, the participation of Cl can significantly reduce the reaction heat required for acetone pyrolysis, thereby reducing the difficulty of carbon source pyrolysis. Furthermore, the introduction of Cl also somewhat accelerates the dehydrogenation process of hydrocarbon groups,[40] which aids in the pyrolysis of acetone along Route II ($CH_3COCH_3 \rightarrow CH_3COCH_2 + H$).

From the kinetic perspective, we calculated the activation energy (E_a) of the rate-limiting step for acetone pyrolysis using the nudged elastic band (NEB) method[43] to further validate the role of Cl in carbon source pyrolysis. It can be seen that the E_a of the rate-limiting step for direct decomposition of acetone ($CH_3CO \rightarrow CH_3 + CO$, Figure 4f) is the same as the reaction heat (ΔE, 1.37 eV), indicating that the kinetic decomposition of CH_3CO needs to overcome the energy barrier of 1.37 eV. However, the E_a and ΔE of the $CH_3CO + Cl \rightarrow CH_3Cl + CO$ reaction involving Cl are 0 and −2.44 eV, respectively (Figure 4g). This reaction occurs spontaneously and simultaneously releases 2.44 eV of heat. The rate-limiting step ($CH_2CO + Cl \rightarrow CH_2Cl + CO$) in Route II involving Cl also owns a low E_a of 0.06 eV (Figure 4h). In addition, further calculations showed that the introduction of Cl was also beneficial for the sufficient decomposition of ethanol (Supplementary Figure 29). To further substantiate the mechanism, we performed HCl gas detection for the exhaust gas with and without CH_2Cl_2. Supplementary Figure 30 and Supplementary Table 5 show the HCl formation after incorporating CH_2Cl_2, which is consistent with the DFT reaction route with the Cl (Figure 4e). Therefore, introducing CH_2Cl_2 to release Cl in the gas phase can enhance the concentration of activated carbon species (C or C_2) formed by carbon source pyrolysis, enabling fast growth of CNTs.

CONCLUSIONS

In summary, we successfully prepared CNTFs with excellent mechanical properties by the CALF-FCCVD method, achieving a tensile strength of up to 5.61 GPa (4.92 N/tex). Theoretical analysis based on the three-level hierarchical model confirms that we can increase the CNT length and improve CNTF mechanical strength by the CALF-FCCVD method. To investigate the effect of Cl and H_2O on the growth of CNTs, we explored the length modulation of CNTs using a horizontal furnace and achieved a length improvement of 731% by the CALF-FCCVD method. Using DFT calculations, we found that the introduction of Cl is beneficial for the sufficient decomposition of carbon sources in thermodynamics and kinetics to generate sufficient active carbon species (C or C_2), leading to the fast growth of CNTs. Besides, the introduction of H_2O is beneficial for the increase in catalyst lifetime. These two factors contribute to improving the utilization of carbon sources during the growth process of CNTs, achieving the preparation of long CNTs. Our study provides a method to optimize the strength of macro CNTFs by modulating the properties of micro constituent CNTs in direct spinning.

ASSOCIATED CONTENT

Supporting Information

The Supporting Information is available free of charge at https://pubs.acs.org/doi/10.1021/jacs.4c01705.

https://doi.org/10.1021/jacs.4c01705
J. Am. Chem. Soc. XXXX, XXX, XXX−XXX

Details about the experimental and computational methods, statistics of CNT length and diameter, linear density and orientation of CNTFs, GC−MS analysis, and mechanical performance (PDF)

As-spun CNTFs prepared by the CALF-FCCVD method (MP4)

AUTHOR INFORMATION

Corresponding Authors

Liu Qian − *School of Materials Science and Engineering, Peking University, Beijing 100871, China*; Email: qianliu-cnc@pku.edu.cn

Xin Gao − *School of Materials Science and Engineering, Peking University, Beijing 100871, China; Beijing Graphene Institute (BGI), Beijing 100095, China;* orcid.org/0000-0001-5360-0796; Email: gaoxin-cnc@pku.edu.cn

Jin Zhang − *Center for Nanochemistry, Beijing Science and Engineering Center for Nanocarbons, Beijing National Laboratory for Molecular Sciences, College of Chemistry and Molecular Engineering and School of Materials Science and Engineering, Peking University, Beijing 100871, China; Beijing Graphene Institute (BGI), Beijing 100095, China;* orcid.org/0000-0003-3731-8859; Email: jinzhang@pku.edu.cn

Authors

Zuncheng Hu − *Center for Nanochemistry, Beijing Science and Engineering Center for Nanocarbons, Beijing National Laboratory for Molecular Sciences, College of Chemistry and Molecular Engineering and School of Materials Science and Engineering, Peking University, Beijing 100871, China*

Xiucai Sun − *Beijing Graphene Institute (BGI), Beijing 100095, China*

Xinshi Zhang − *Center for Nanochemistry, Beijing Science and Engineering Center for Nanocarbons, Beijing National Laboratory for Molecular Sciences, College of Chemistry and Molecular Engineering and School of Materials Science and Engineering, Peking University, Beijing 100871, China; Beijing Graphene Institute (BGI), Beijing 100095, China*

Xiangzheng Jia − *Department of Engineering Mechanics, School of Civil Engineering, Wuhan University, Wuhan 430072, China*

Xueting Feng − *Center for Nanochemistry, Beijing Science and Engineering Center for Nanocarbons, Beijing National Laboratory for Molecular Sciences, College of Chemistry and Molecular Engineering, Peking University, Beijing 100871, China*

Mingwei Cui − *Center for Nanochemistry, Beijing Science and Engineering Center for Nanocarbons, Beijing National Laboratory for Molecular Sciences, College of Chemistry and Molecular Engineering and School of Materials Science and Engineering, Peking University, Beijing 100871, China*

Enlai Gao − *Department of Engineering Mechanics, School of Civil Engineering, Wuhan University, Wuhan 430072, China;* orcid.org/0000-0003-1960-0260

Complete contact information is available at: https://pubs.acs.org/10.1021/jacs.4c01705

Author Contributions

⊥Z.H. and X.S. contributed equally to this work.

Notes

The authors declare no competing financial interest.

ACKNOWLEDGMENTS

We thank Suzhou Institute of Nano-Tech and Nano-Bionics, Chinese Academy of Sciences for fiber preparation support. This work was supported by the Ministry of Science and Technology of China (2022YFA1203302, 2022YFA1203304, and 2018YFA0703502), the National Natural Science Foundation of China (grant nos. 52021006, 52102032), the Strategic Priority Research Program of CAS (XDB36030100), and the Beijing National Laboratory for Molecular Sciences (BNLMS-CXTD-202001). X.G. thanks the National Natural Science Foundation of China (grant no. 52302034). The numerical calculations in this work were done on the supercomputing system in the Supercomputing Center of Wuhan University.

REFERENCES

(1) Iijima, S. Helical microtubules of graphitic carbon. *Nature* **1991**, *354* (6348), 56−58.

(2) Zhang, R. F.; Wen, Q.; Qian, W. Z.; Su, D. S.; Zhang, Q.; Wei, F. Superstrong ultra long carbon nanotubes for mechanical energy storage. *Adv. Mater.* **2011**, *23* (30), 3387−3391.

(3) Peng, B.; Locascio, M.; Zapol, P.; Li, S. Y.; Mielke, S. L.; Schatz, G. C.; Espinosa, H. D. Measurements of near-ultimate strength for multiwalled carbon nanotubes and irradiation-induced crosslinking improvements. *Nat. Nanotechnol.* **2008**, *3* (10), 626−631.

(4) Wu, Y. Z.; Zhao, X. W.; Shang, Y. Y.; Chang, S. L.; Dai, L. X.; Cao, A. Y. Application-driven carbon nanotube functional materials. *ACS Nano* **2021**, *15* (5), 7946−7974.

(5) Vigolo, B.; Penicaud, A.; Coulon, C.; Sauder, C.; Pailler, R.; Journet, C.; Bernier, P.; Poulin, P. Macroscopic fibers and ribbons of oriented carbon nanotubes. *Science* **2000**, *290* (5495), 1331−1334.

(6) Jiang, K. L.; Li, Q. Q.; Fan, S. S. Nanotechnology: Spinning continuous carbon nanotube yarns - Carbon nanotubes weave their way into a range of imaginative macroscopic applications. *Nature* **2002**, *419* (6909), 801−801.

(7) Zhu, H. W.; Xu, C. L.; Wu, D. H.; Wei, B. Q.; Vajtai, R.; Ajayan, P. M. Direct synthesis of long single-walled carbon nanotube strands. *Science* **2002**, *296* (5569), 884−886.

(8) Ding, F.; Bolton, K.; Rosen, A. Nucleation and growth of single-walled carbon nanotubes: A molecular dynamics study. *J. Phys. Chem. B* **2004**, *108* (45), 17369−17377.

(9) Rao, R.; Liptak, D.; Cherukuri, T.; Yakobson, B. I.; Maruyama, B. In situ evidence for chirality-dependent growth rates of individual carbon nanotubes. *Nat. Mater.* **2012**, *11* (3), 213−216.

(10) Gao, E. L.; Lu, W. B.; Xu, Z. P. Strength loss of carbon nanotube fibers explained in a three-level hierarchical model. *Carbon* **2018**, *138*, 134−142.

(11) Zhou, T.; Niu, Y. T.; Li, Z.; Li, H. F.; Yong, Z. Z.; Wu, K. J.; Zhang, Y. Y.; Li, Q. W. The synergetic relationship between the length and orientation of carbon nanotubes in direct spinning of high-strength carbon nanotube fibers. *Mater. Des.* **2021**, *203*, No. 109557.

(12) Zhong, X. H.; Li, Y. L.; Liu, Y. K.; Qiao, X. H.; Feng, Y.; Liang, J.; Jin, J.; Zhu, L.; Hou, F.; Li, J. Y. Continuous multilayered carbon nanotube yarns. *Adv. Mater.* **2010**, *22* (6), 692−696.

(13) Wang, J. N.; Luo, X. G.; Wu, T.; Chen, Y. High-strength carbon nanotube fibre-like ribbon with high ductility and high electrical conductivity. *Nat. Commun.* **2014**, *5* (1), 3848.

(14) Wang, J. J.; Zhao, J. N.; Zhao, L. M.; Lu, Q.; Zhou, T.; Yong, Z. Z.; Wang, P. F.; Zhang, X. H.; Li, Q. W. Interfacial-bubbling-induced nondestructive expansion to reconstruct superstrong and multifunctional carbon nanotube fibers. *Carbon* **2021**, *184*, 24−33.

(15) Lee, J.; Lee, D.-M.; Jung, Y.; Park, J.; Lee, H. S.; Kim, Y.-K.; Park, C. R.; Jeong, H. S.; Kim, S. M. Direct spinning and densification method for high-performance carbon nanotube fibers. *Nat. Commun.* **2019**, *10* (1), 2962.

(16) Miao, M. H.; Hawkins, S. C.; Cai, J. Y.; Gengenbach, T. R.; Knott, R.; Huynh, C. P. Effect of gamma-irradiation on the

mechanical properties of carbon nanotube yarns. *Carbon* **2011**, *49* (14), 4940−4947.
(17) Wen, Y. Y.; Jian, M. Q.; Huang, J. K.; Luo, J. J.; Qian, L.; Zhang, J. Carbonene fibers: Toward next-generation fiber materials. *Nano Lett.* **2022**, *22* (15), 6035−6047.
(18) Ma, W. J.; Liu, L. Q.; Yang, R.; Zhang, T. H.; Zhang, Z.; Song, L.; Ren, Y.; Shen, J.; Niu, Z. Q.; Zhou, W. Y.; Xie, S. S. Monitoring a micromechanical process in macroscale carbon nanotube films and fibers. *Adv. Mater.* **2009**, *21* (5), 603−608.
(19) Yamada, T.; Maigne, A.; Yudasaka, M.; Mizuno, K.; Futaba, D. N.; Yumura, M.; Iijima, S.; Hata, K. Revealing the secret of water-assisted carbon nanotube synthesis by microscopic observation of the interaction of water on the catalysts. *Nano Lett.* **2008**, *8* (12), 4288−4292.
(20) Dong, L. Y.; Park, J. G.; Leonhardt, B. E.; Zhang, S. L.; Liang, R. Continuous synthesis of double-walled carbon nanotubes with water-assisted floating catalyst chemical vapor deposition. *Nanomaterials* **2020**, *10* (2), 365.
(21) Yang, W. X.; Liu, X. J.; Yue, X. Y.; Jia, J. B.; Guo, S. J. Bamboo-like carbon nanotube/Fe3C nanoparticle hybrids and their highly efficient catalysis for oxygen reduction. *J. Am. Chem. Soc.* **2015**, *137* (4), 1436−1439.
(22) Gommans, H. H.; Alldredge, J. W.; Tashiro, H.; Park, J.; Magnuson, J.; Rinzler, A. G. Fibers of aligned single-walled carbon nanotubes: Polarized Raman spectroscopy. *J. Appl. Phys.* **2000**, *88* (5), 2509−2514.
(23) Davis, V. A.; Parra-Vasquez, A. N. G.; Green, M. J.; Rai, P. K.; Behabtu, N.; Prieto, V.; Booker, R. D.; Schmidt, J.; Kesselman, E.; Zhou, W.; Fan, H.; Adams, W. W.; Hauge, R. H.; Fischer, J. E.; Cohen, Y.; Talmon, Y.; Smalley, R. E.; Pasquali, M. True solutions of single-walled carbon nanotubes for assembly into macroscopic materials. *Nat. Nanotechnol.* **2009**, *4* (12), 830−834.
(24) Liu, Y. D.; Kumar, S. Recent progress in fabrication, structure, and properties of carbon fibers. *Polym. Rev.* **2012**, *52* (3), 234−258.
(25) Liu, F.; Wang, Q.; Zhai, G.; Xiang, H.; Zhou, J.; Jia, C.; Zhu, L.; Wu, Q.; Zhu, M. Continuously processing waste lignin into high-value carbon nanotube fibers. *Nat. Commun.* **2022**, *13* (1), 5755.
(26) Shang, Y. Y.; Wang, Y.; Li, S. H.; Hua, C. F.; Zou, M. C.; Cao, A. Y. High-strength carbon nanotube fibers by twist-induced self-strengthening. *Carbon* **2017**, *119*, 47−55.
(27) Zhang, X.; De Volder, M.; Zhou, W.; Issman, L.; Wei, X.; Kaniyoor, A.; Portas, J. T.; Smail, F.; Wang, Z.; Wang, Y.; Liu, H.; Zhou, W.; Elliott, J.; Xie, S.; Boies, A. Simultaneously enhanced tenacity, rupture work, and thermal conductivity of carbon nanotube fibers by raising effective tube portion. *Sci. Adv.* **2022**, *8* (50), No. eabq3515.
(28) Cho, Y. S.; Lee, J. W.; Kim, J.; Jung, Y.; Yang, S. J.; Park, C. R. Superstrong carbon nanotube yarns by developing multiscale bundle structures on the direct spin-line without post-treatment. *Adv. Sci.* **2023**, *10* (2), No. 2204250.
(29) Kinoshita, T.; Karita, M.; Chikyu, N.; Nakano, T.; Inoue, Y. Enhancement of catalytic activity by addition of chlorine in chemical vapor deposition growth of carbon nanotube forests. *Carbon* **2022**, *196*, 391−400.
(30) Zhang, M.; Atkinson, K. R.; Baughman, R. H. Multifunctional carbon nanotube yarns by downsizing an ancient technology. *Science* **2004**, *306* (5700), 1358−1361.
(31) Zhang, X. F.; Li, Q. W.; Holesinger, T. G.; Arendt, P. N.; Huang, J. Y.; Kirven, P. D.; Clapp, T. G.; DePaula, R. F.; Liao, X. Z.; Zhao, Y. H.; Zheng, L. X.; Peterson, D. E.; Zhu, Y. T. Ultrastrong, stiff, and lightweight carbon-nanotube fibers. *Adv. Mater.* **2007**, *19* (23), 4198−4201.
(32) Jia, J. J.; Zhao, J. N.; Xu, G.; Di, J. T.; Yong, Z. Z.; Tao, Y. Y.; Fang, C. O.; Zhang, Z. G.; Zhang, X. H.; Zheng, L. X.; Li, Q. W. A comparison of the mechanical properties of fibers spun from different carbon nanotubes. *Carbon* **2011**, *49* (4), 1333−1339.
(33) Zhang, X. F.; Li, Q. W.; Tu, Y.; Li, Y. A.; Coulter, J. Y.; Zheng, L. X.; Zhao, Y. H.; Jia, Q. X.; Peterson, D. E.; Zhu, Y. T. Strong carbon-nanotube fibers spun from long carbon-nanotube arrays. *Small* **2007**, *3* (2), 244−248.
(34) Liu, K.; Zhu, F.; Liu, L.; Sun, Y. H.; Fan, S. S.; Jiang, K. L. Fabrication and processing of high-strength densely packed carbon nanotube yarns without solution processes. *Nanoscale* **2012**, *4* (11), 3389−3393.
(35) Miaudet, P.; Badaire, S.; Maugey, M.; Derre, A.; Pichot, V.; Launois, P.; Poulin, P.; Zakri, C. Hot-drawing of single and multiwall carbon nanotube fibers for high toughness and alignment. *Nano Lett.* **2005**, *5* (11), 2212−2215.
(36) Taylor, L. W.; Dewey, O. S.; Headrick, R. J.; Komatsu, N.; Peraca, N. M.; Wehmeyer, G.; Kono, J.; Pasquali, M. Improved properties, increased production, and the path to broad adoption of carbon nanotube fibers. *Carbon* **2021**, *171*, 689−694.
(37) Tsentalovich, D. E.; Headrick, R. J.; Mirri, F.; Hao, J. L.; Behabtu, N.; Young, C. C.; Pasquali, M. Influence of carbon nanotube characteristics on macroscopic fiber properties. *ACS Appl. Mater. Interfaces* **2017**, *9* (41), 36189−36198.
(38) Jiao, X. Y.; Shi, C.; Zhao, Y. M.; Xu, L. L.; Liu, S. K.; Hou, P. X.; Liu, C.; Cheng, H. M. Efficient fabrication of high-quality single-walled carbon nanotubes and their macroscopic conductive fibers. *ACS Nano* **2022**, *16* (12), 20263−20271.
(39) Wu, Y. P.; Won, Y. S. Pyrolysis of chloromethanes. *Combust. Flame* **2000**, *122* (3), 312−326.
(40) Xu, S.; Cheng, T.; Yan, Q.; Shen, C.; Yu, Y.; Lin, C.-T.; Ding, F.; Zhang, J. Chloroform-assisted rapid growth of vertical graphene array and its application in thermal interface materials. *Adv. Sci.* **2022**, *9* (15), No. 2200737.
(41) Hata, K.; Futaba, D. N.; Mizuno, K.; Namai, T.; Yumura, M.; Iijima, S. Water-assisted highly efficient synthesis of impurity-free single-walled carbon nanotubes. *Science* **2004**, *306* (5700), 1362−1364.
(42) Zaleski, D. P.; Sivaramakrishnan, R.; Weller, H. R.; Seifert, N. A.; Bross, D. H.; Ruscic, B.; Moore, K. B.; Elliott, S. N.; Copan, A. V.; Harding, L. B.; Klippenstein, S. J.; Field, R. W.; Prozument, K. Substitution reactions in the pyrolysis of acetone revealed through a modeling, experiment, theory paradigm. *J. Am. Chem. Soc.* **2021**, *143* (8), 3124−3142.
(43) Mills, G.; Jonsson, H.; Schenter, G. K. Reversible work transition state theory: application to dissociative adsorption of hydrogen. *Surf. Sci.* **1995**, *324* (2−3), 305−337.

https://doi.org/10.1021/jacs.4c01705
J. Am. Chem. Soc. XXXX, XXX, XXX−XXX

Supplementary Information

Kinetic modulation of carbon nanotube growth in direct spinning for high-strength carbon nanotube fibers

Zuncheng Hu[1,2#], Xiucai Sun[3#], Xinshi Zhang[1,2,3], Xiangzheng Jia[4], Xueting Feng[1], Mingwei Cui[1,2], Enlai Gao[4], Liu Qian[2]*, Xin Gao[2,3]*, and Jin Zhang[1,2,3]*

[1]Center for Nanochemistry, Beijing Science and Engineering Center for Nanocarbons, Beijing National Laboratory for Molecular Sciences, College of Chemistry and Molecular Engineering, Peking University, Beijing, 100871, China.

[2]School of Materials Science and Engineering, Peking University, Beijing, 100871, China.

[3]Beijing Graphene Institute (BGI), Beijing, 100095, China.

[4]Department of Engineering Mechanics, School of Civil Engineering, Wuhan University, Wuhan, 430072, China.

[#]These authors contributed equally to this work: Zuncheng Hu and Xiucai Sun.

Experimental Section

Synthesis of carbon nanotube fibers (CNTFs)

CNTFs were continuously synthesized by a direct spinning method based on floating catalyst chemical vapor deposition (FCCVD) at 1300 °C. The vertical reactor has an alumina tube with an inner diameter of 90 mm and a heating zone of 760 mm. The catalyst solution contains ferrocene (4.43 mg/mL), thiophene (14.19 mg/mL), acetone, ethanol, water and dichloromethane. The catalyst solution is injected into the reaction system by a syringe. The injection rate of the catalyst solution is 30 mL/h, and the reaction atmosphere includes argon and hydrogen. The reactor was sealed by a water bath. The carbon nanotube (CNT) aerogels generated from the vertical furnace were immersed in water and densified to obtain as-spun CNTFs. The CNTFs were directly spun on a bobbin with a spinning rate of 23 m/min. The wet CNTFs on the bobbin were dried at 400 °C on air by a roll-to-roll method.

Chlorosulphonic acid (CSA) stretching treatment of CNTFs

The as-spun CNTFs were immersed into CSA solution for 5 min with a stretching ratio of 5%. Then the fibers were introduced into the acetone bath for densification, after that the fibers were dried and collected on a winder.

Rolling treatment of CNTFs

We applied conventional rolling to further enhance the packing density of the CNTs in the fiber (ZK2015OR, Dongguan Chi Division Precision Machinery Co., Ltd., China). During this process, the top of the as-prepared film on the Al foil substrate was covered with another piece of Al foil. Such a sample was rolled between two rollers running in

opposite directions. Before each rolling, the two rollers were adjusted so that they were in touch with each other and there was no gap between them from visualization of naked eyes. To improve rolling homogeneity, the same sample was rolled several times.

CNTFs characterization

The tensile tests were conducted on a Nano-Tensile Tester-testing system (SHIMADZU EZ-LX 5N) at a loading rate of 1 mm/min. Samples for tensile test were prepared by sticking fibers to rectangular paper frames with a gauge length of 10 mm using epoxy glue. Regarding the acquisition of the cross-sectional area of fibers: For as-spun CNTFs and CNTFs after CSA stretching, the diameter (d) is obtained by twisting the CNTFs into an approximately circular shape and observing them with an optical microscope or scanning electron microscope (SEM). Then the cross-sectional area (S) is calculated based on $S=\frac{\pi d^2}{4}$. During mechanical testing, the fibers in the test section were not subjected to twisting treatment. For the rolled fibers, the cross-sectional areas of CNTFs were obtained using Image J software from cross-sectional SEM images. For the observation, the CNTFs were cut using focused ion beam (FIB) system (Helios G4 UX, Thermo Fisher). Considering the tilt angle of the sample (52°), the cross-sectional area was calculated by dividing the area obtained from the SEM image by cosine of 38°. SEM images and energy dispersive X-ray spectroscopy (EDS) mapping images were obtained on a Hitachi S4800 SEM equipped with APOLLO XP EDS operating at 5 kV and 10 kV respectively. Transmission electron microscope (TEM) images of CNTFs cross section were obtained using JEM-2100F at 200 kV. Raman spectra of CNTFs were measured by Horiba HR800 Raman system with 532

nm excitation. Polarized Raman spectra were recorded on a Horiba HR Evolution Raman system with a 532 nm exciting laser. A rotatable polaroid glass was used to adjust the polarization direction of Raman exciting laser with the rotation range of 0-360°. The content of the residual catalyst particles of CNTFs was measured by thermogravimetric analysis (TGA) (Q600 SDT). The linear density (tex was defined as the mass in grams per 1000 m) was obtained by measuring the mass of a known length (5-meter-long) of fiber and calculating the mass per unit length as g/km, a unit otherwise known as a tex.

Synthesis of CNTs

CNTs were prepared continuously by FCCVD at 1100 ℃. The horizontal reactor has a quartz tube with an inner diameter of 22 mm and a heating zone of 305 mm. The catalyst solution contains ferrocene, thiophene, acetone, water and dichloromethane. The catalyst solution is injected into the reaction system by a syringe. The injection rate of the catalyst solution is 10 μL/min, and the reaction atmosphere includes argon, hydrogen and ethanol vapor (argon bubbling). The total flow of argon and hydrogen is about 1000 standard cubic centimeters per minute (sccm). The length of the CVD furnace is 410 mm. The catalysts take 9 seconds to flow through the CVD furnace. The experiment was conducted in four different carbon source concentrations of reaction atmosphere, namely, 30 sccm EtOH (30 sccm argon through an ethanol bubbler) +1000 sccm H_2 (C1), 30 sccm EtOH+500 sccm H_2+500 sccm Ar (C2), 60 sccm EtOH+500 sccm H_2+500 sccm Ar (C3) and 90 sccm EtOH+500 sccm H_2+500 sccm Ar (C4). Placing a silicon chip at the exit of the furnace (below 400 ℃) to hold the CNTs after

growth. It needs 30 s to obtain trace amounts of CNTs with almost no cross-linking for convenient length statistics. When characterizing the quality of CNTs, generally growing for about 15 min to obtain enough CNTs to obtain strong intensity of Raman signals.

Length statistics of CNTs and fitting

Under each growth condition, using Image J software to count the length of 100 uncrosslinked CNTs in the SEM images. We used log-normal distribution to fit the experiment data. The probability density function of log-normal distribution is given by

$$p(x) = \frac{1}{x\sigma\sqrt{2\pi}} e^{-\frac{(\ln(x-\mu))^2}{2\sigma^2}}, x>0 \quad (1)$$

where σ and μ are parameters, and x is a random variable.

CNTs characterization

SEM images were obtained on a Hitachi S4800 SEM operated at 1 kV. Raman spectra of CNTs were collected from Jovin Yvon-Horiba LabRam systems with 532 nm excitation (beam spot of ~1 μm). X-ray photoelectron spectroscopy (XPS) was performed on an AXIS Supra X-ray Photoelectron Spectrometer (Kratos Analytical Ltd.) with Al Kα (1486.6 eV) as the X-ray source. TEM was conducted on Tecnai F20 Super-Twin equipped with Gatan 1095.IS OneView CCD operating at 200 kV. Gas chromatography-mass spectrometer (GC-MS) tests were carried out using Shimadzu GCMS-TQ8050. Atomic force microscope (AFM) images were obtained using a Dimension Icon microscope (Bruker).

Theoretical analysis for mechanical strength enhancement of CNTFs

To investigate the change of CNTs length in our prepared fibers, mechanism analysis was conducted based on the three-level hierarchical model[1], which rationalizes the multi-scale degradation of mechanical performance at the individual CNT, CNT bundle, and CNTF levels. For individual CNTs with length l, the failure probability can be well modeled using a two-parameter Weibull distribution function $F(\sigma) = 1\text{-}\exp[-(\sigma/\sigma_l)^m]$, where m is the shape parameter related to the type and density of defects, σ_l is the scale parameter which indicates the statistical nature of tensile strength. Therefore, the tensile strength of defective CNTs with length l can be denoted as $\sigma_1 = \sigma_l\Gamma(1+1/m)$, where $\sigma_l = \sigma_{l0}(l/l_0)^{-1/m}$, σ_{l0} is the scale parameter of Weibull distribution for CNT with length l_0. The primary reduction factor α_1 can be deduced as

$$\alpha_1 = \frac{\sigma_1}{\sigma_0} = \frac{\sigma_{l0}}{\sigma_0}\left(\frac{l}{l_0}\right)^{-\frac{1}{m}}\Gamma\left(1+\frac{1}{m}\right) \tag{2}$$

For randomly staggered CNT bundles, the strength can be determined by the tension-shear model. With this model, a critical overlap length l_c was defined, which determines whether CNTs occur inter-failure ($l \geq 2l_c$) or intra-slippage ($l < 2l_c$). The fiber we prepared exhibits ductile fracture (Supplementary Fig. 31), which is mainly caused by intra-slippage between CNTs. Therefore, by assuming that l_0 is uniformly distributed between 0 to l, the average tensile strength can be derived as the average value, that is, $\sigma_2 = l\sigma_1/8l_c$. The secondary reduction factor α_2 can be deduced as

$$\alpha_2 = \frac{\sigma_2}{\sigma_1} = \frac{l}{8l_c} \tag{3}$$

For CNTFs, the fiber is considered as an assembly of the bundles, where a wavy model is developed to map the tensile strength of the CNT bundles to CNTFs. The tertiary factor α_3 mainly depends on the packing density and orientation degree of

CNTFs. For the fiber after post-treatment, the $I_{G\parallel}/I_{G\perp}$ of the fiber obtained under Fe-Cl-H_2O (1:1.6:207) is 1.82, which is similar to the fiber obtained under Fe-H_2O (1:207) ($I_{G\parallel}/I_{G\perp}$=1.95, Supplementary Fig. 9). Moreover, the cross-sectional SEM images (Supplementary Fig. 10e, f) and TEM images (Supplementary Fig. 2) of CNTFs also show that the fibers obtained under Fe-Cl-H_2O (1:1.6:207) and Fe-H_2O (1:207) after rolling both are very tight. Hence, α_3 can be regarded as a constant.

In combination with the above theoretical model, we can calculate the change in CNTs length from experimental strength. The introduction of Cl promotes the tensile strength from 3.35 GPa (Supplementary Fig. 11c) to 5.27 GPa (Supplementary Fig. 11d). Based on our three-level hierarchical model, that is

$$\frac{\sigma'}{\sigma} = \frac{\alpha_1'\alpha_2'\alpha_3}{\alpha_1\alpha_2\alpha_3} = \left(\frac{l'}{l}\right)^{(m\text{-}1)/m} = 1.57 \quad (4)$$

Considering the representative value of m (2-10)[1], the range of l'/l is from 1.7 to 2.5, suggesting that our strategy increases the length of CNTs by 70%-150% and improves the mechanical properties of CNTFs.

Density functional theory (DFT) calculations

All DFT calculations were performed using the Vienna ab initio Simulation Package (VASP)[2, 3] within the projector-augmented wave basis[4]. The generalized gradient approximation proposed by Perdew, Burke, and Ernzerhof is selected for the exchange-correlation potential[5]. The cut-off energy for plane wave is set to 450 eV. The energy criterion is set to 10^{-5} eV in iterative solution of the Kohn-Sham equation. The carbon source molecules and the reaction intermediates were put in boxes of size 20 Å×20 Å×20 Å to compute the molecular energies in order to avoid artificial interaction

between periodic images and model the pyrolysis process of the carbon source in the gas phase. The Brillouin zone integration is performed using a 1×1×1 k-mesh. All the structures are relaxed until the residual forces on the atoms have declined to less than 0.05 eV/Å. The free energy of intermediate species during acetone and ethanol pyrolysis was obtained from:

$$G = E_{molecular} + \Delta E_{ZPE} - T\Delta S \quad (5)$$

where $E_{molecular}$ is the energy of carbon source molecules or the reaction intermediates, T is the temperature, ΔE_{ZPE} and ΔS are the difference in zero-point energy and entropy change, respectively.

The transition states were searched using the climbing image nudged elastic band (CI-NEB) method integrated into VASP[6]. Frequency analysis was carried out to verify the transition states. The reaction barrier E_a and reaction energy ΔE are calculated as:

$$E_a = E_{TS} - E_{IS} \quad (6)$$

$$\Delta E = E_{FS} - E_{IS} \quad (7)$$

where E_{IS}, E_{TS}, and E_{FS} represent the energies of the initial state (IS), transition state (TS), and final state (FS), respectively.

Supplementary Tables

Supplementary Table 1. Mechanical properties of CNTFs prepared by the CALF-FCCVD method.

Material	Mass (g)	Length (m)	Linear density (tex)	Tensile force (N)	Displacement (mm)	Specific strength (N/tex)
As-spun CNTFs	0.0036	5	0.72	0.908	0.384	1.261
				0.918	0.426	1.275
				0.930	0.520	1.292
				0.903	0.498	1.254
				0.928	0.474	1.289
CNTFs after CSA stretching	0.0025	5	0.5	2.037	0.451	4.074
				1.920	0.393	3.84
				2.290	0.489	4.58
				2.085	0.446	4.17
CNTFs after CSA stretching and rolling	0.0025	5	0.5	2.168	0.529	4.336
				2.326	0.471	4.652
				2.459	0.606	4.918
				2.288	0.548	4.576

Supplementary Table 2. Comparison of tensile strength, specific strength, and elongation at break of as-prepared CNTFs with commercial carbon fibers and CNTFs prepared by FCCVD spinning, forest spinning, and wet spinning.

Material	Method	Tensile strength (GPa)	Specific strength (N/tex)	Elongation at break (%)	Reference
CNTFs	FCCVD spinning	5.27	4.62	5.38	This work
CNTFs	FCCVD spinning	1.33	0.89	5.8	7
CNTFs	FCCVD spinning	3.35	\	10	8
CNTFs	FCCVD spinning	4.34	2.8	10	9
CNTFs	FCCVD spinning	1.2	\	8	10
CNTFs	FCCVD spinning	3.5	3.1	5	11
CNTFs	FCCVD spinning	4.60	3.30	4	12
CNTFs	FCCVD spinning	1.94	5.5	5.85	13
CNTFs	Forest spinning	1.37	1.12	1.34	14
CNTFs	Forest spinning	0.46	0.575	8.8	15
CNTFs	Forest spinning	3.3	\	9	16
CNTFs	Forest spinning	1.23	1.602	2	17
CNTFs	Forest spinning	1.91	\	7.02	18
CNTFs	Forest spinning	1.6	\	1.4	19
CNTFs	Wet spinning	1.8	\	12	20
CNTFs	Wet spinning	4.2	2.1	3.5	21
CNTFs	Wet spinning	0.15	0.11	3	22
CNTFs	Wet spinning	2.4	1.54	1.8	23
CNTFs	Wet spinning	0.745	0.573	6.5	24
Carbon fibers	Toray T300	3.53	2.01	1.5	25
Carbon fibers	Toray M55J	4.02	2.10	0.8	25

Supplementary Table 3. The GC-MS quantitative analysis of CH_4, C_2H_6, C_2H_4, and C_2H_2 in the reaction exhaust under the condition of Fe, Fe-Cl (1:2), Fe-H_2O (1:2), and Fe-Cl-H_2O (1:2:2).

Condition	Gas	Volume concentration (%)
Fe	CH_4	7.45
	C_2H_6	0.00648
	C_2H_4	0.176
	C_2H_2	0.0583
Fe-Cl (1:2)	CH_4	9.53
	C_2H_6	0.00464
	C_2H_4	0.217
	C_2H_2	0.116
Fe-H_2O (1:2)	CH_4	7.57
	C_2H_6	0.0106
	C_2H_4	0.235
	C_2H_2	0.110
Fe-Cl-H_2O (1:2:2)	CH_4	7.12
	C_2H_6	0.00632
	C_2H_4	0.117
	C_2H_2	0.0333

Supplementary Table 4. Stepwise reactions and associated free energy increments (ΔG) during pyrolysis of acetone and ethanol carbon sources.

Carbon source	Route	Reaction	ΔG (eV)
CH_3COCH_3	w/o Cl-Route I	(I) $CH_3COCH_3 \rightarrow CH_3CO+CH_3$	2.82
		(II) $CH_3CO \rightarrow CH_3+CO$	6.59
		(III) $CH_3 \rightarrow CH_2+H$	4.19
		(IV) $CH_2 \rightarrow CH+H$	3.91
		(V) $CH \rightarrow C+H$	4.19
	w/ Cl-Route I	(I') $CH_3COCH_3+Cl \rightarrow CH_3CO+CH_3Cl$	-0.14
		(II') $CH_3CO+Cl \rightarrow CH_3Cl+CO$	3.63
		(III') $CH_3Cl \rightarrow CH_2+HCl$	2.61
		(IV') $CH_2+Cl \rightarrow CH+HCl$	-0.63
		(V') $CH+Cl \rightarrow C+HCl$	-0.35
	w/ Cl-Route II	(I'') $CH_3COCH_3+Cl \rightarrow CH_3COCH_2+HCl$	-0.28
		(II'') $CH_3COCH_2+Cl \rightarrow CH_2CO+CH_3Cl$	-3.25
		(III'') $CH_2CO+Cl \rightarrow CH_2Cl+CO$	6.23
		(IV'') $CH_2Cl \rightarrow CH+HCl$	2.76
		(V'') $CH+Cl \rightarrow C+HCl$	-0.35
C_2H_5OH	w/o Cl-Route	(I) $C_2H_5OH \rightarrow C_2H_5+OH$	3.30
		(II) $C_2H_5 \rightarrow C_2H_4+H$	1.06
		(III) $C_2H_4 \rightarrow C_2H_3+H$	4.72
		(IV) $C_2H_3 \rightarrow C_2H_2+H$	0.44
		(V) $C_2H_2 \rightarrow C_2H+H$	5.39
		(VI) $C_2H \rightarrow C_2+H$	5.43
		(VII) $C_2 \rightarrow C+C$	6.79
	w/ Cl-Route	(I') $C_2H_5OH \rightarrow C_2H_5+OH$	3.30
		(II') $C_2H_5+Cl \rightarrow C_2H_4+HCl$	-3.48
		(III') $C_2H_4+Cl \rightarrow C_2H_3+HCl$	0.18
		(IV') $C_2H_3+Cl \rightarrow C_2H_2+HCl$	-4.10
		(V') $C_2H_2+Cl \rightarrow C_2H+HCl$	0.85
		(VI') $C_2H+Cl \rightarrow C_2+HCl$	0.89
		(VII') $C_2 \rightarrow C+C$	6.79

Supplementary Table 5. The pH value of exhaust gas absorption solution under different conditions.

Condition	pH
Fe	4.03
Fe-Cl (1:2)	0.85

Note: The pH value is measured using pH meter (PHS-3C) at 25 ℃.

Supplementary Table 6. The carbon source concentration corresponding to the optimal CNTs length under different conditions.

Condition	The optimal carbon source concentration
Fe	30 sccm EtOH+1000 sccm H_2
Fe-Cl (1:0.2)	60 sccm EtOH+500 sccm H_2+500 sccm Ar
Fe-Cl (1:0.5)	60 sccm EtOH+500 sccm H_2+500 sccm Ar
Fe-Cl (1:1)	60 sccm EtOH+500 sccm H_2+500 sccm Ar
Fe-Cl (1:2)	60 sccm EtOH+500 sccm H_2+500 sccm Ar
Fe-Cl (1:4)	60 sccm EtOH+500 sccm H_2+500 sccm Ar
Fe-H_2O (1:1)	30 sccm EtOH+1000 sccm H_2
Fe-H_2O (1:2)	60 sccm EtOH+500 sccm H_2+500 sccm Ar
Fe-H_2O (1:4)	90 sccm EtOH+500 sccm H_2+500 sccm Ar
Fe-Cl-H_2O (1:2:1)	60 sccm EtOH+500 sccm H_2+500 sccm Ar
Fe-Cl-H_2O (1:2:2)	60 sccm EtOH+500 sccm H_2+500 sccm Ar
Fe-Cl-H_2O (1:2:4)	60 sccm EtOH+500 sccm H_2+500 sccm Ar

Note: Fe: the condition of Cl and H_2O are not introduced; Fe-Cl (1:0.2): the molar ratio of Fe to Cl is 1:0.2; the naming method is similar in other cases. The experiments were conducted in four different carbon source concentrations of reaction atmosphere, namely, 30 sccm EtOH +1000 sccm H_2 (C1), 30 sccm EtOH+500 sccm H_2+500 sccm Ar (C2), 60 sccm EtOH+500 sccm H_2+500 sccm Ar (C3) and 90 sccm EtOH+500 sccm H_2+500 sccm Ar (C4).

Supplementary Figures

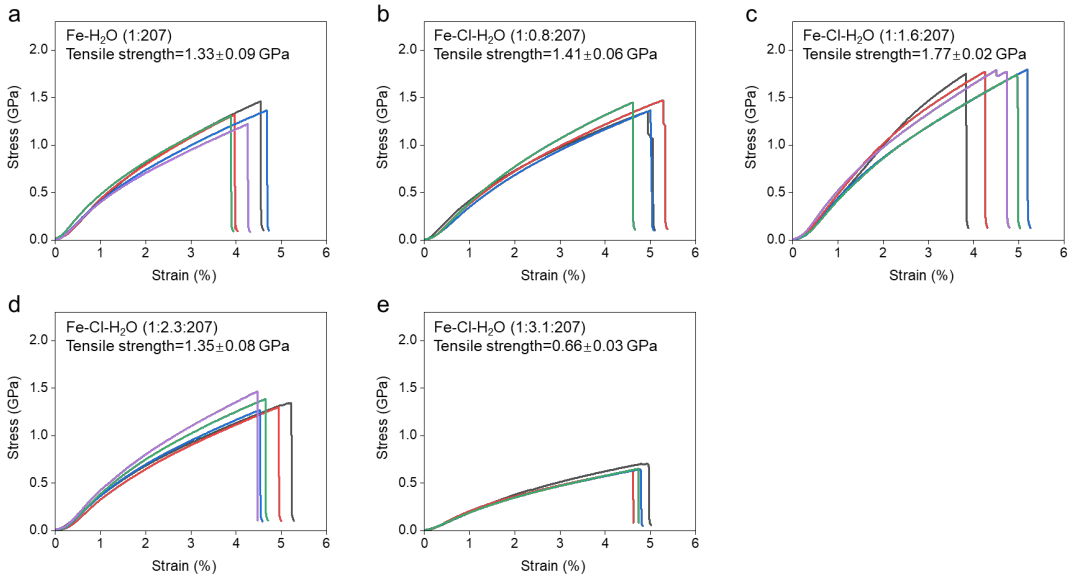

Supplementary Figure 1. Strength of as-spun CNTFs. Stress-strain curves of as-spun CNTFs obtained under **a** Fe-H_2O (1:207), **b** Fe-Cl-H_2O (1:0.8:207), **c** Fe-Cl-H_2O (1:1.6:207), **d** Fe-Cl-H_2O (1:2.3:207) and **e** Fe-Cl-H_2O (1:3.1:207). Number of replicated measurements (n) is as follows: Fe-H_2O (1:207) (n=5), Fe-Cl-H_2O (1:0.8:207) (n=4), Fe-Cl-H_2O (1:1.6:207) (n=5), Fe-Cl-H_2O (1:2.3:207) (n=5), Fe-Cl-H_2O (1:3.1:207) (n=4).

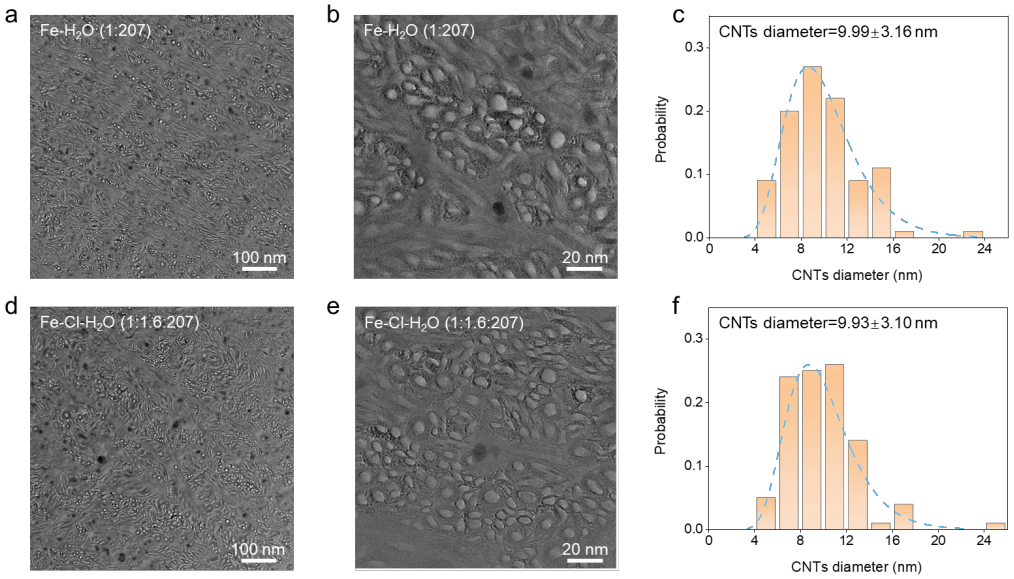

Supplementary Figure 2. Diameter analysis of CNTs in as-prepared fibers. a, b Cross-sectional TEM images of CNTFs obtained under Fe-H_2O (1:207) after CSA stretching and rolling and **c** the corresponding diameter distribution of the CNTs measured from 100 CNTs by TEM. **d, e** Cross-sectional TEM images of CNTFs obtained under Fe-Cl-H_2O (1:1.6:207) after CSA stretching and rolling and **f** the corresponding diameter distribution of the CNTs measured from 100 CNTs by TEM.

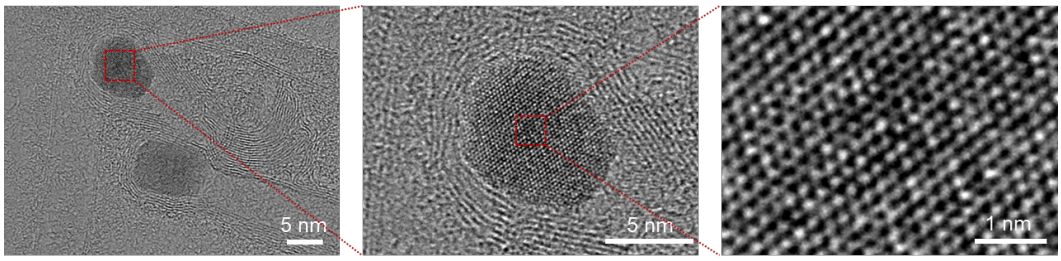

Supplementary Figure 3. TEM images of nanoparticles in as-spun CNTFs.

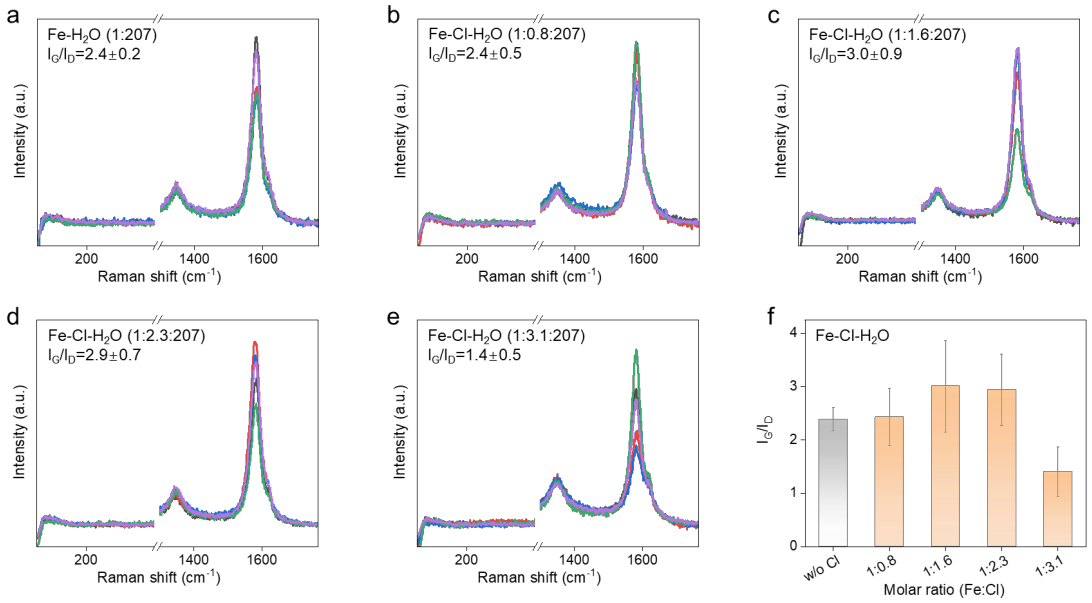

Supplementary Figure 4. Quality of as-spun CNTFs. On the basis of Fe-H_2O (1:207), **a-e** Raman spectra and **f** I_G/I_D values of CNTFs under different Cl contents. Error bars indicate the standard deviation. Number of replicates for each experimental condition is 5.

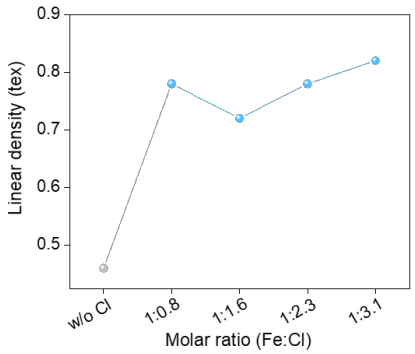

Supplementary Figure 5. Linear density of as-spun CNTFs. Linear density of CNTFs under different Cl contents.

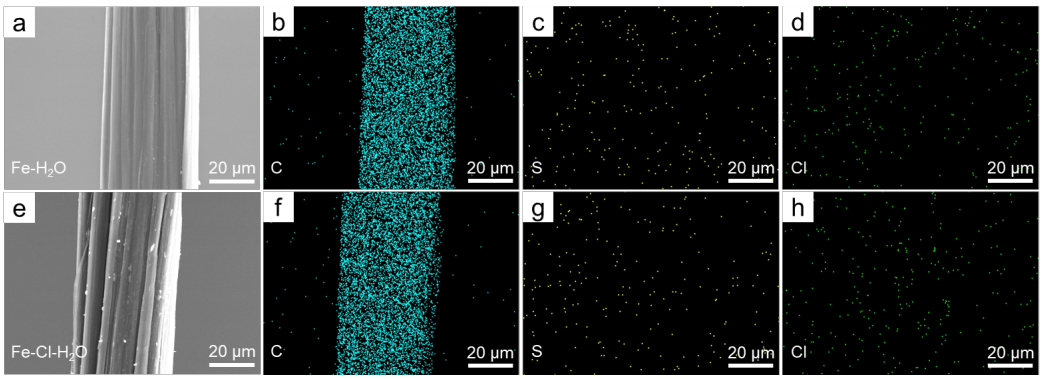

Supplementary Figure 6. SEM and EDS characterization of as-spun CNTFs. a SEM image and **b-d** elemental mapping images of the CNTFs obtained under Fe-H_2O (1:207). **e** SEM image and **f-h** elemental mapping images of the CNTFs obtained under Fe-Cl-H_2O (1:1.6:207).

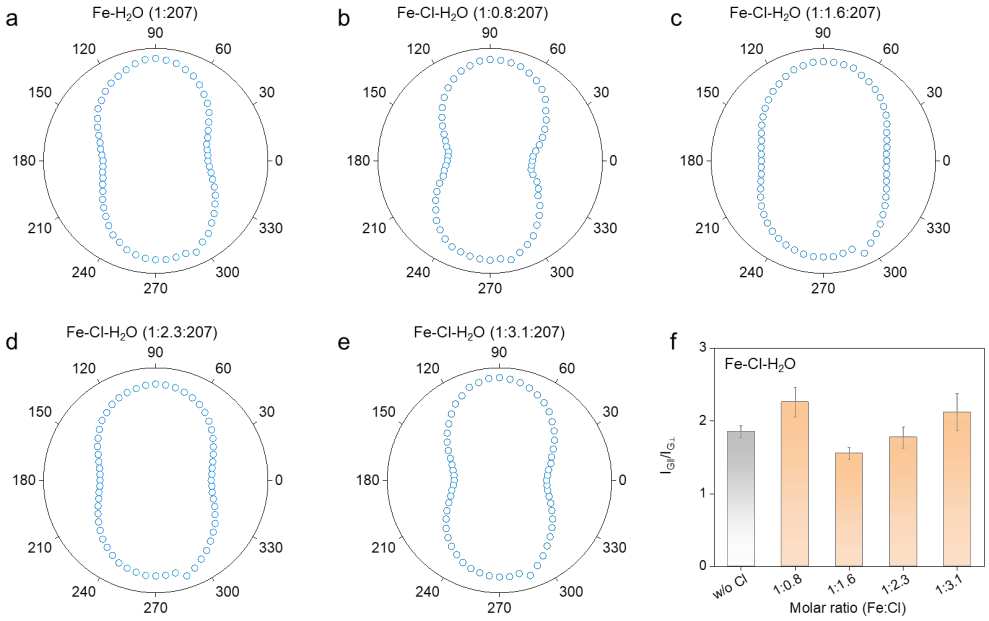

Supplementary Figure 7. Orientation characterization of as-spun CNTFs. On the basis of Fe-H_2O (1:207), **a-e** polarized Raman spectra and **f** $I_{G\parallel}/I_{G\perp}$ values of CNTFs under different Cl contents. Error bars indicate the standard deviation. Number of replicates for each experimental condition is as follows: Fe-H_2O (1:207) (n=4), Fe-Cl-H_2O (1:0.8:207) (n=5), Fe-Cl-H_2O (1:1.6:207) (n=5), Fe-Cl-H_2O (1:2.3:207) (n=4), Fe-Cl-H_2O (1:3.1:207) (n=5).

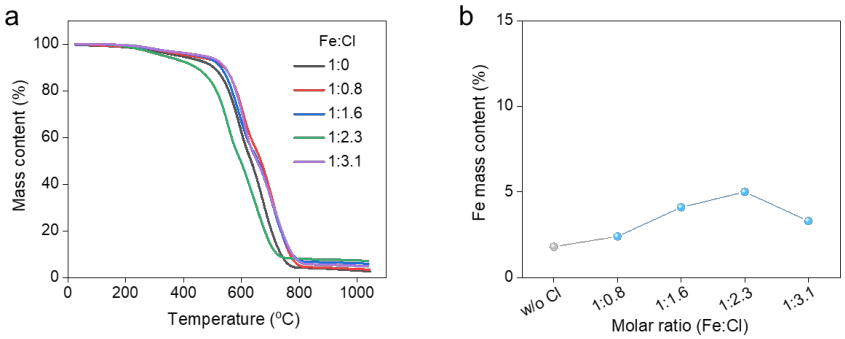

Supplementary Figure 8. Purity characterization of as-spun CNTFs. On the basis of Fe-H_2O (1:207), **a** TGA curves of as-spun CNTFs and **b** contents of residual Fe of CNTFs under different Cl contents.

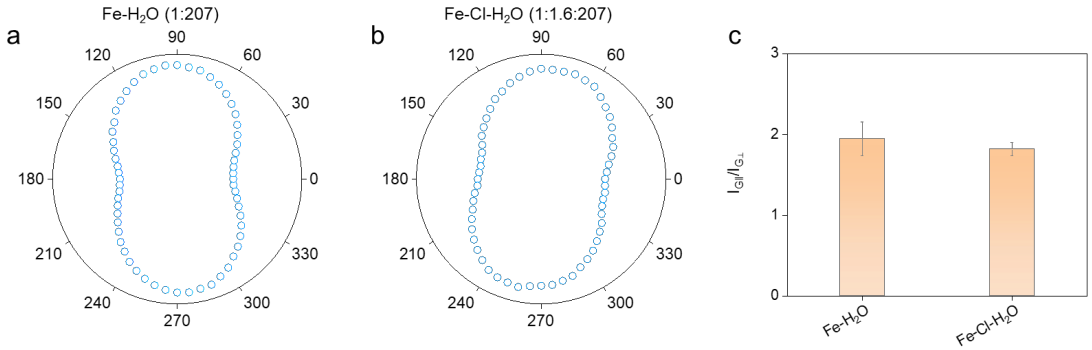

Supplementary Figure 9. Orientation characterization of CNTFs after CSA stretching. a, b Polarized Raman spectra and **c** $I_{G\parallel}/I_{G\perp}$ values of CNTFs after CSA stretching. Error bars indicate the standard deviation. Number of replicates for each experimental condition is as follows: Fe-H_2O (1:207) (n=5), Fe-Cl-H_2O (1:1.6:207) (n=5).

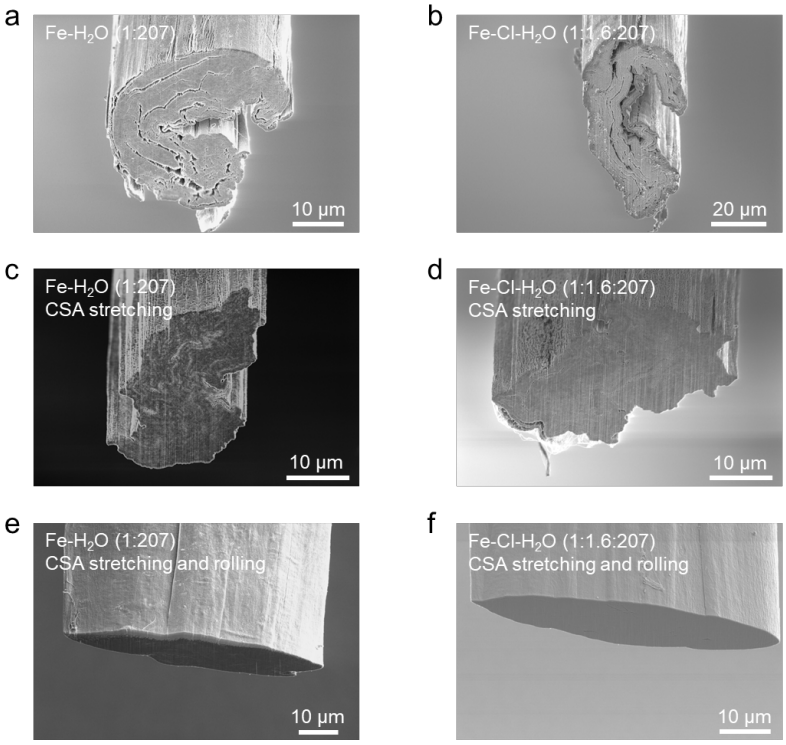

Supplementary Figure 10. Cross-sectional SEM images of CNTFs. Cross-sectional SEM images of **a, b** as-spun CNTFs, **c, d** CNTFs after CSA stretching and **e, f** CNTFs after CSA stretching and rolling obtained under Fe-H_2O (1:207) and Fe-Cl-H_2O (1:1.6:207).

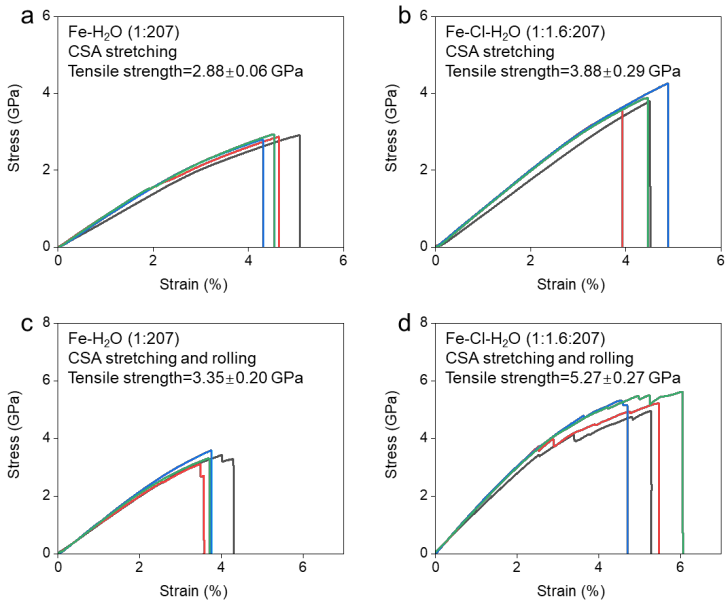

Supplementary Figure 11. Strength of CNTFs after post-treatment. Stress-strain curves of CNTFs obtained under **a** Fe-H_2O (1:207) after CSA stretching, **b** Fe-Cl-H_2O (1:1.6:207) after CSA stretching, **c** Fe-H_2O (1:207) after CSA stretching and rolling, and **d** Fe-Cl-H_2O (1:1.6:207) after CSA stretching and rolling. Number of replicates for each experimental condition is 4.

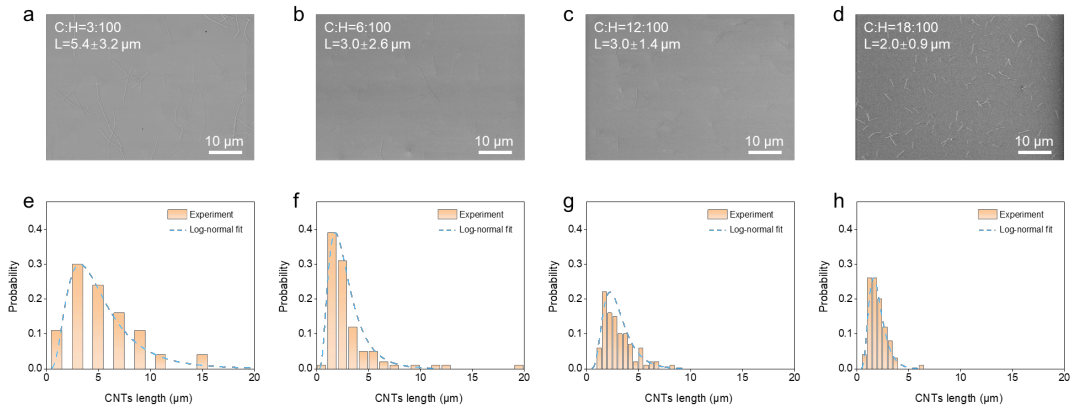

Supplementary Figure 12. Length modulation of CNTs with condition of Fe. a-d SEM images and **e-h** the corresponding length statistical distribution of CNTs under different C:H ratios (denote the molar ratio of EtOH to H_2 as C:H).

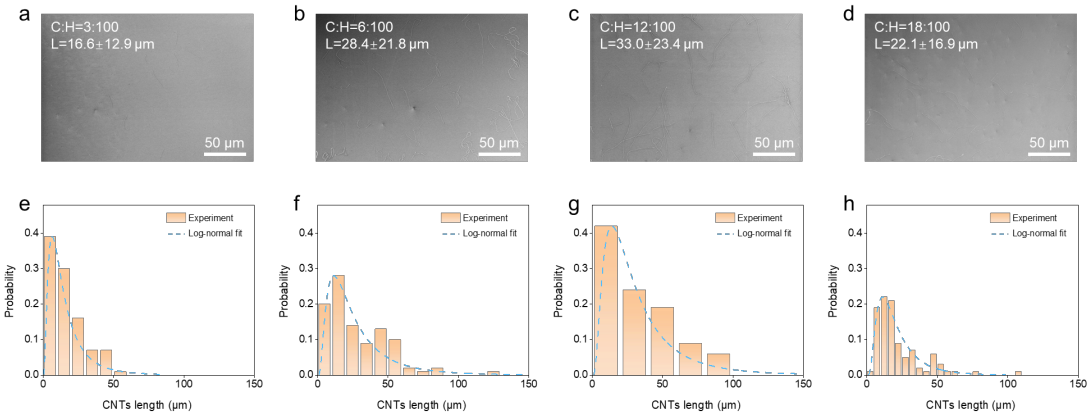

Supplementary Figure 13. Length modulation of CNTs with condition of Fe-Cl (1:1). a-d SEM images and **e-h** the corresponding length statistical distribution of CNTs under different C:H ratios.

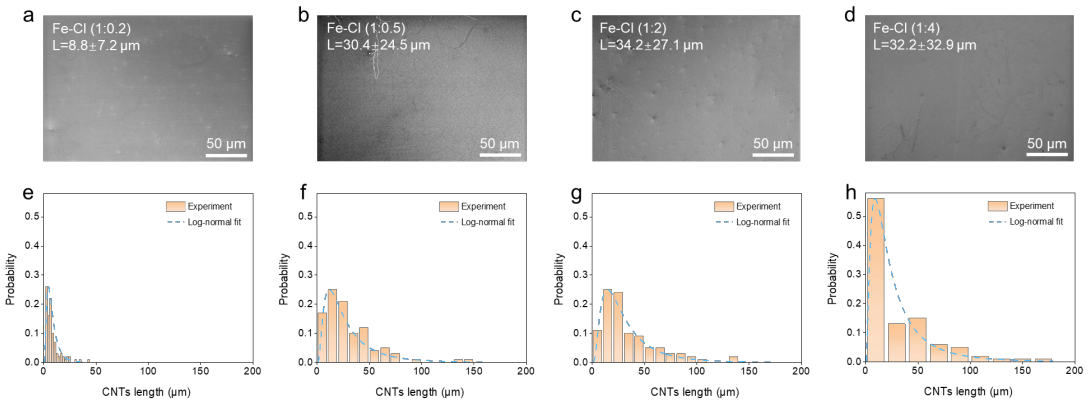

Supplementary Figure 14. Length modulation of CNTs with different Cl contents. **a-d** SEM images and **e-h** the corresponding length statistical distribution of CNTs under optimal C:H ratios.

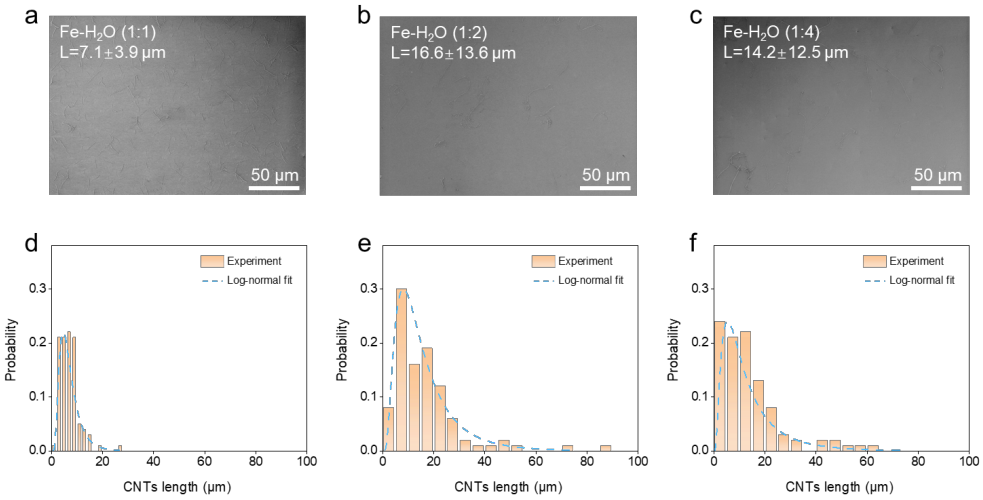

Supplementary Figure 15. Length modulation of CNTs with different H_2O contents. a-c SEM images and **d-f** the corresponding length statistical distribution of CNTs under optimal C:H ratios.

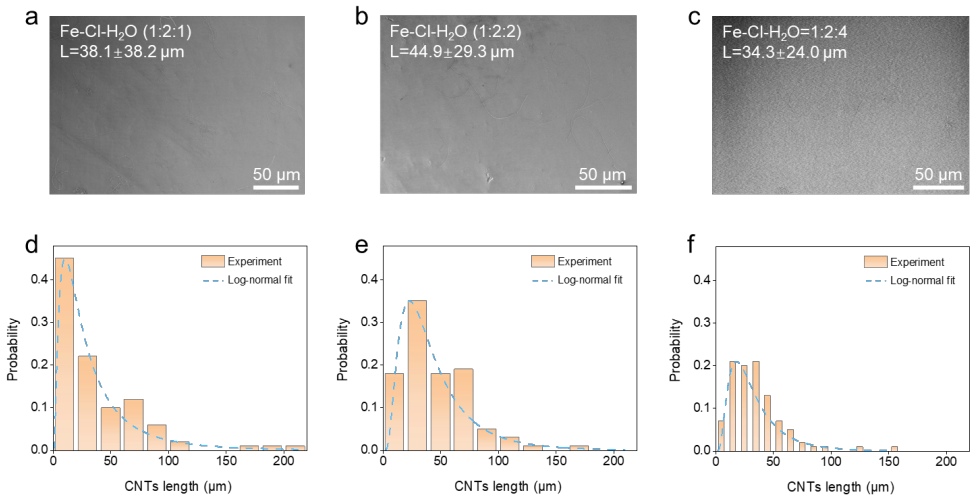

Supplementary Figure 16. Length modulation of CNTs with different H_2O contents on the basis of Fe-Cl (1:2). a-c SEM images and **d-f** the corresponding length statistical distribution of CNTs under optimal C:H ratios.

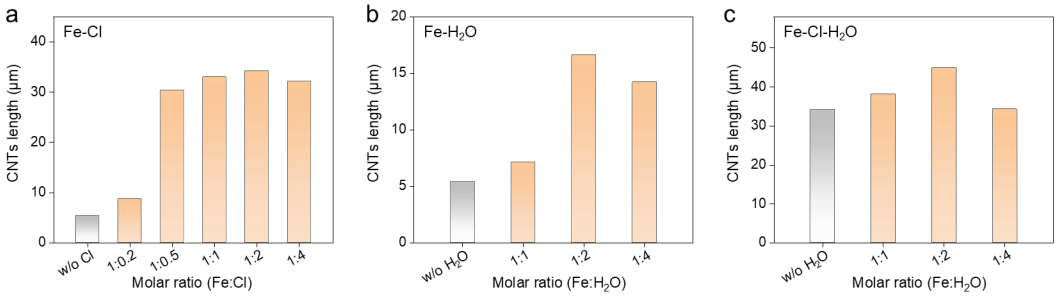

Supplementary Figure 17. Comparison of CNTs length under different conditions. The optimal average length (refer to the optimal length under four carbon source atmospheres) of CNTs under conditions of **a** Fe-Cl, **b** Fe-H_2O and **c** Fe-Cl-H_2O.

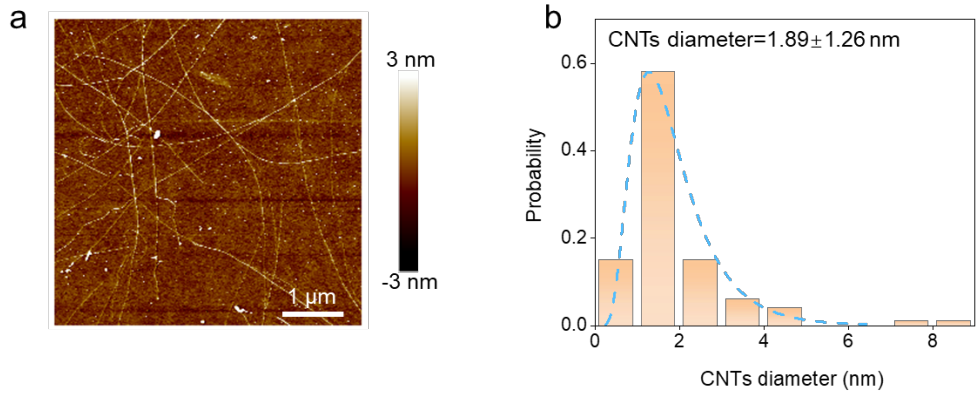

Supplementary Figure 18. Diameter of CNTs. a Typical AFM image of CNTs for length regulation experiment and **b** diameter distribution of the CNTs measured from 100 CNTs by AFM observation.

Note: When conducting the length modulation experiment of CNTs, due to the low injection rate (10 μL/min) of the catalyst solution (ferrocene concentration is 30 mg/mL) and short growth time (~30 s), the total amount of Fe atoms injected into the reactor is only 8.06×10^{-7} mol and the probability of CNTs entangled into CNT bundles in the gas phase is relatively low. Therefore, we can approximately consider that the CNT in the SEM image used for statistical length is an individual CNT (average diameter=1.89 nm) rather than a large CNT bundle.

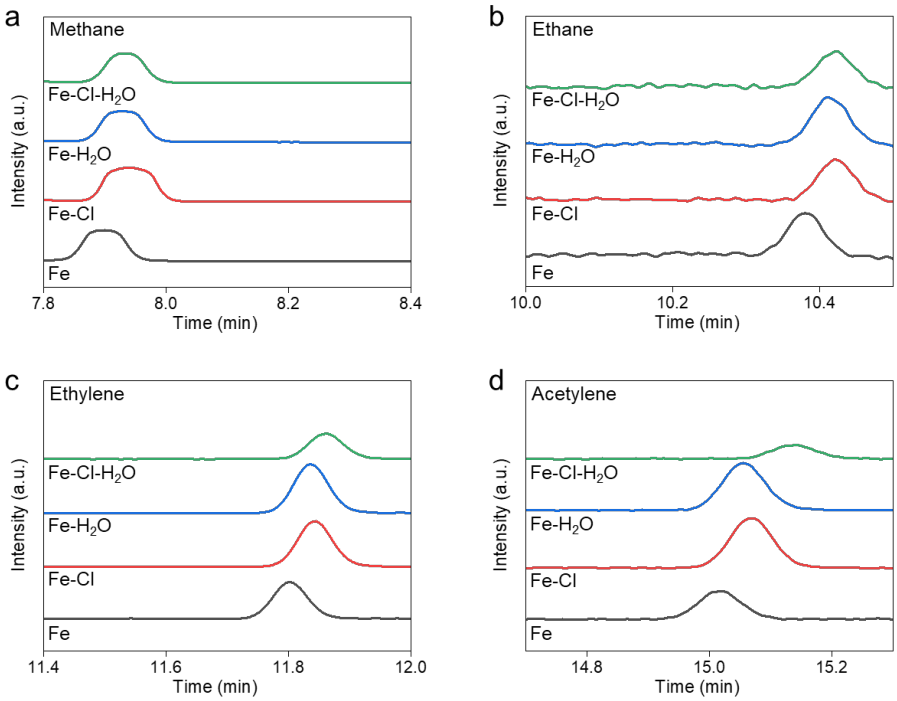

Supplementary Figure 19. GC-MS analysis of different carbon-containing gases. The GC-MS analysis of **a** CH_4, **b** C_2H_6, **c** C_2H_4 and **d** C_2H_2 in reaction exhaust at growth atmosphere of 60 sccm EtOH+500 sccm H_2+500 sccm Ar under the condition of Fe, Fe-Cl (1:2), Fe-H_2O (1:2) and Fe-Cl-H_2O (1:2:2).

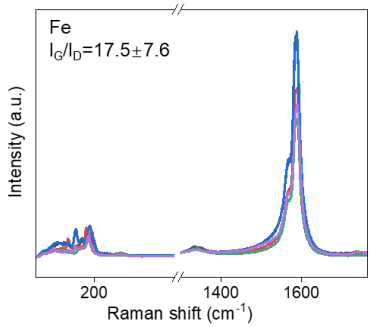

Supplementary Figure 20. Quality of CNTs under the condition of Fe. Raman spectra of CNTs grown at 60 sccm EtOH+500 sccm H_2+500 sccm Ar under the condition of Fe. Number of replicates is 5.

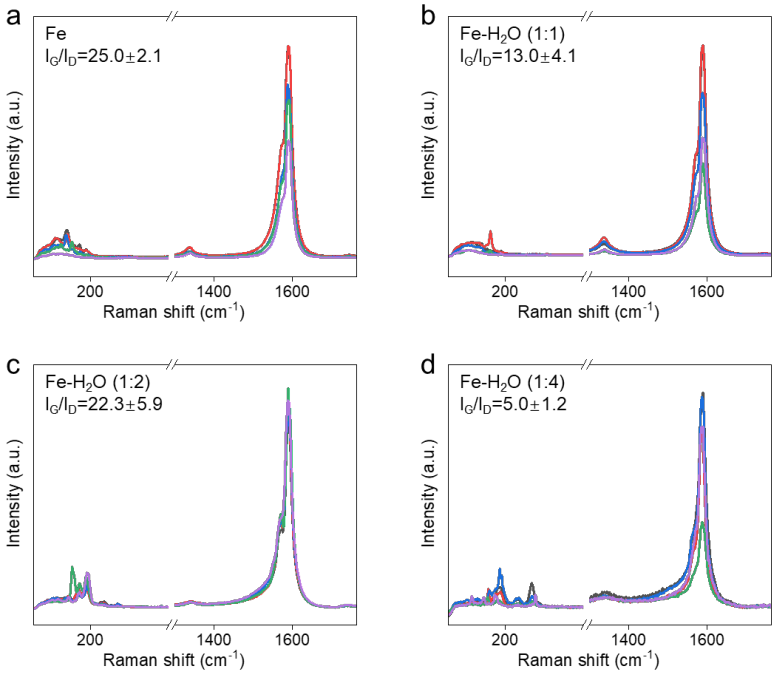

Supplementary Figure 21. Quality of CNTs under different H_2O contents. Raman spectra of CNTs at optimal C:H ratios under **a** Fe, **b** Fe-H_2O (1:1), **c** Fe-H_2O (1:2) and **d** Fe-H_2O (1:4). Number of replicates for each experimental condition is 5.

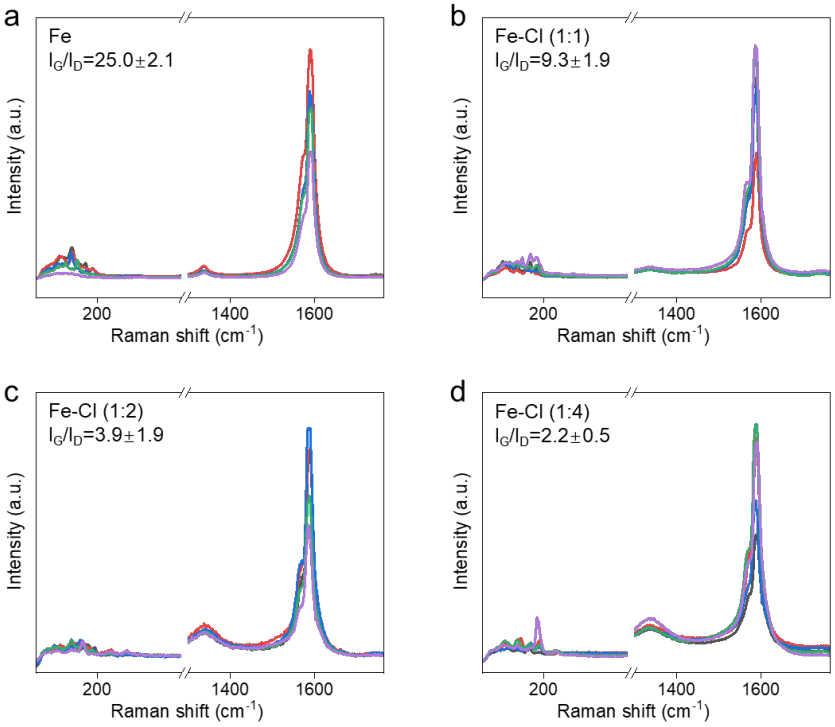

Supplementary Figure 22. Quality of CNTs under different Cl contents. Raman spectra of CNTs at optimal C:H ratios under **a** Fe, **b** Fe-Cl (1:1), **c** Fe-Cl (1:2) and **d** Fe-Cl (1:4). Number of replicates for each experimental condition is 5.

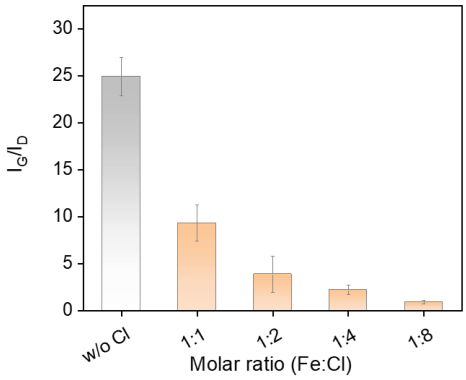

Supplementary Figure 23. Comparison of the CNT quality under different contents of Cl. I_G/I_D values from Raman spectra of CNTs at optimal C:H ratios under different Fe to Cl ratio in molar. Error bars indicate the standard deviation. Number of replicates for each experimental condition is 5.

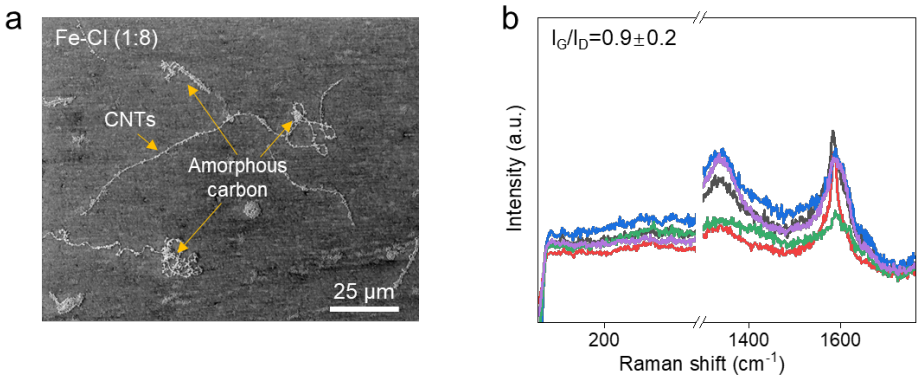

Supplementary Figure 24. Growth results of CNTs under Fe-Cl (1:8). a SEM image and **b** Raman spectra of CNTs.
Note: Excess Cl resulted in more amorphous carbon formation.

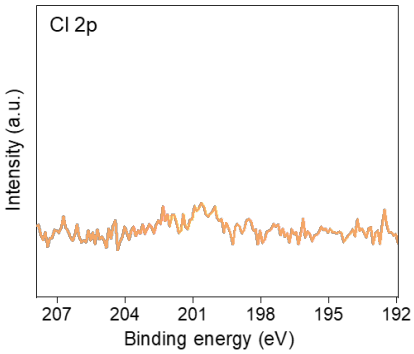

Supplementary Figure 25. XPS characterization of CNTs. XPS spectrum in Cl 2p region of the silicon chip substrate surface after CNTs grown under Fe-Cl (1:8).

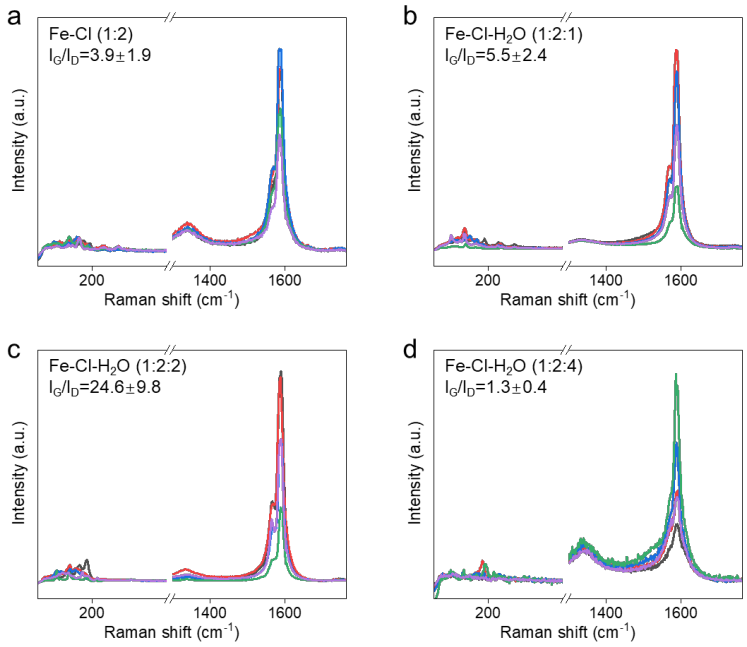

Supplementary Figure 26. Quality of CNTs under different H_2O contents on the basis of Fe-Cl (1:2). Raman spectra of CNTs at optimal C:H ratios under **a** Fe-Cl (1:2), **b** Fe-Cl-H_2O (1:2:1), **c** Fe-Cl-H_2O (1:2:2) and **d** Fe-Cl-H_2O (1:2:4). Number of replicates for each experimental condition is 5.

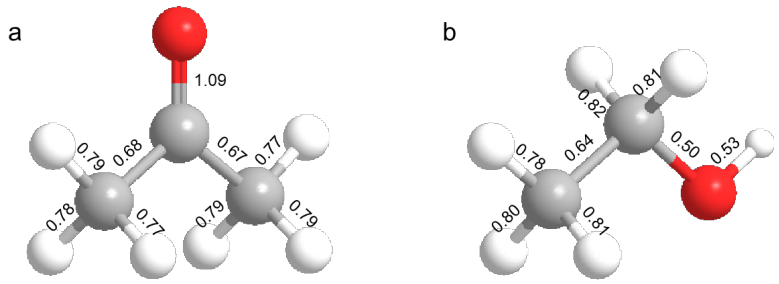

Supplementary Figure 27. Overlap populations of chemical bonds in acetone and ethanol molecules. Red, grey and white spheres are oxygen, carbon and hydrogen atoms, respectively.

Note: The numbers in the figure indicate the overlap populations of chemical bonds in the molecules of two carbon sources, acetone and ethanol. The smaller the number, the easier it is for the bond to break. For acetone, it is easiest to break C-C bond first. For ethanol, it is easiest to break C-O bond first.

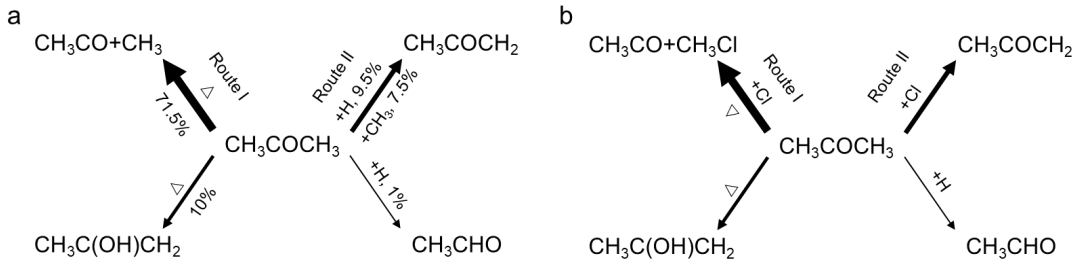

Supplementary Figure 28. Decomposition route of acetone adopted from literature[26]. a The decomposition route of acetone without introducing Cl. **b** The decomposition route of acetone with introducing Cl.

Note: In order to understand the role of Cl in the fast growth of CNTs, we follow the decomposition route of acetone in the literature[26]. When Cl is not introduced, the preferential C-C bonds cleavage process ($CH_3COCH_3 \rightarrow CH_3CO+CH_3$) in acetone cracking accounts for the largest proportion, which is consistent with the inferences from the calculations of overlap populations of chemical bonds in acetone (Supplementary Fig. 27a). As a result, the preferential C-C bond breaking in acetone procedure serves as the main pathway of our investigation and is designated Route I for simplicity in documentation. Besides, since the CVD atmosphere is abundant in H and CH_3 radicals, which collide with the acetone molecules to induce C-H bond breaking, a small amount of acetone will also have a reaction pathway that preferentially breaks H, and is therefore considered concurrently as a secondary pathway (Route II). Additionally, other reaction paths that may occur in the heating of acetone with H are not considered in this paper due to their low probability.

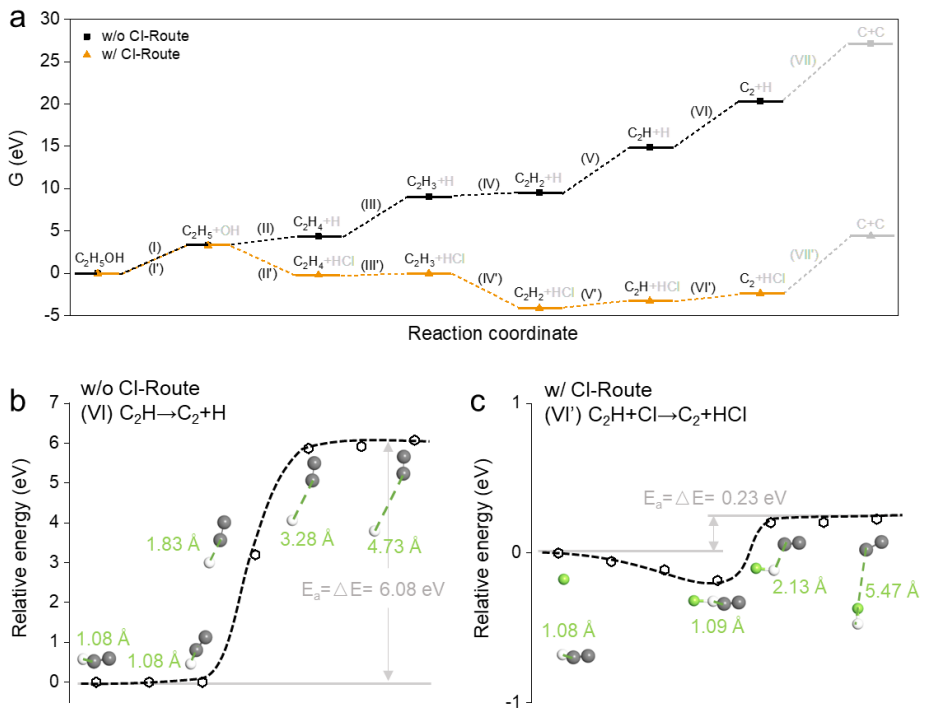

Supplementary Figure 29. Thermodynamic and kinetic analysis of ethanol decomposition. a Calculated free energy of ethanol progressive pyrolysis. **b** Energy profile of the intermediate process ($C_2H \rightarrow C_2+H$) in the reaction route without introducing Cl. **c** Energy profile of the intermediate process ($C_2H+Cl \rightarrow C_2+HCl$) in the reaction route involving Cl. E_a represents activation energy, and ΔE represents reaction heat. The green numbers represent the distance between the carbon atom and the hydrogen atom connected by green dashed line. Green, grey and white spheres are chlorine, carbon and hydrogen atoms, respectively.

Note: According to the overlap populations of chemical bonds in ethanol (Supplementary Fig. 27b), the C-O bond has a minimum value of 0.50, and therefore the ethanol breaks the C-O bond ($C_2H_5OH \rightarrow C_2H_5+OH$) first, which is consistent with the result in the literature[27]. Due to the excessive ΔG of $C_2 \rightarrow C+C$ (6.79 eV), we approximately believe that the reaction is difficult to achieve, thus ethanol ultimately pyrolysis to provide C_2 in the gas phase. Thermodynamic studies also show that the complete pyrolysis of ethanol to C_2 with the assistance of Cl is exothermic, and has a substantially lower ΔG value (-2.36 eV) than the process without Cl (20.35 eV). Meanwhile, further kinetic calculations revealed that the activation energy of the rate-limiting step of ethanol pyrolysis ($C_2H+Cl \rightarrow C_2+HCl$) in the presence of Cl assistance is 0.23 eV (Supplementary Fig. 29c), which was significantly lower than that of the rate-limiting step ($C_2H \rightarrow C_2+H$) without the introduction of Cl (6.08 eV, Supplementary Fig. 29b). From this, it is clear that adding Cl does encourage a more thorough conversion of ethanol to C_2 reactive species in the gas phase.

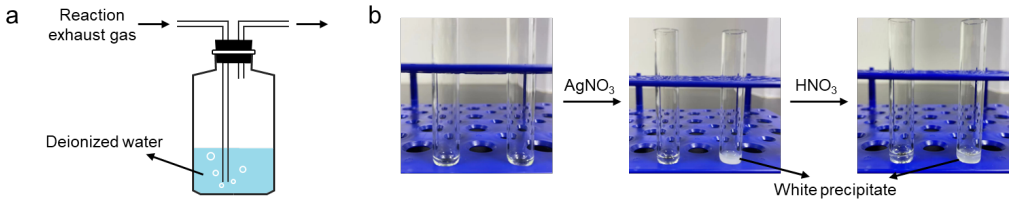

Supplementary Figure 30. Detection of HCl in tail gas. a Schematic showing the potential HCl enrichment in tail gas. **b** Qualitative detection of Cl^- (The left test tube is under Fe condition and the right test tube is under Fe-Cl condition).

Note: In order to enrich the potential HCl gas, an appropriate amount of deionized water is added to the washing cylinder and collected for a long time. After adding $AgNO_3$ solution and dilute HNO_3 solution to the tail gas absorption solution under Fe-Cl condition, white precipitates were generated, while under Fe condition, there was no white precipitate generated in the tail gas absorption solution. Considering that the pH value of the tail gas absorption solution under Fe-Cl condition is significantly lower than that under Fe condition (Supplementary Table 5), it can be inferred that HCl was generated after introducing Cl into the reaction solution, which is consistent with the theoretical calculation results.

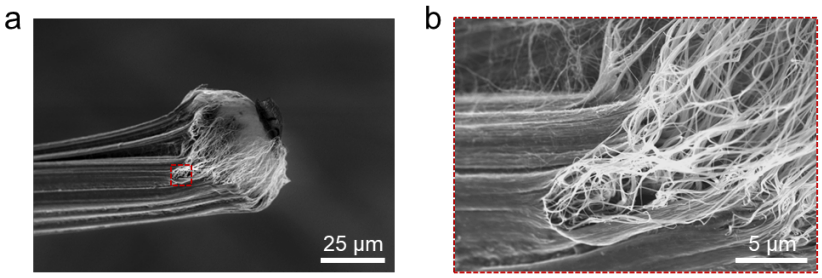

Supplementary Figure 31. Fracture morphology images of CNTFs. a SEM image of the CNTFs fracture. **b** Enlarged image of CNTFs fracture (red frame in **a**).

Supplementary References

1. Gao, E. L.; Lu, W. B.; Xu, Z. P., Strength loss of carbon nanotube fibers explained in a three-level hierarchical model. *Carbon* **2018,** *138*, 134-142.
2. Blöchl, P. E., Projector augmented-wave method. *Phys. Rev. B* **1994,** *50* (24), 17953-17979.
3. Kresse, G.; Furthmuller, J., Efficient iterative schemes for ab initio total-energy calculations using a plane-wave basis set. *Phys. Rev. B* **1996,** *54* (16), 11169-11186.
4. Kresse, G.; Joubert, D., From ultrasoft pseudopotentials to the projector augmented-wave method. *Phys. Rev. B* **1999,** *59* (3), 1758-1775.
5. Perdew, J. P.; Burke, K.; Ernzerhof, M., Generalized gradient approximation made simple. *Phys. Rev. Lett.* **1996,** *77* (18), 3865-3868.
6. Mills, G.; Jonsson, H.; Schenter, G. K., Reversible work transition state theory: Application to dissociative adsorption of hydrogen. *Surf. Sci.* **1995,** *324* (2-3), 305-337.
7. Liu, F. Y.; Wang, Q. Q.; Zhai, G. X.; Xiang, H. X.; Zhou, J. L.; Jia, C.; Zhu, L. P.; Wu, Q. L.; Zhu, M. F., Continuously processing waste lignin into high-value carbon nanotube fibers. *Nat. Commun.* **2022,** *13* (1), 5755.
8. Shang, Y. Y.; Wang, Y.; Li, S. H.; Hua, C. F.; Zou, M. C.; Cao, A. Y., High-strength carbon nanotube fibers by twist-induced self-strengthening. *Carbon* **2017,** *119*, 47-55.
9. Wang, J. N.; Luo, X. G.; Wu, T.; Chen, Y., High-strength carbon nanotube fibre-like ribbon with high ductility and high electrical conductivity. *Nat. Commun.* **2014,** *5* (1), 3848.
10. Zhu, H. W.; Xu, C. L.; Wu, D. H.; Wei, B. Q.; Vajtai, R.; Ajayan, P. M., Direct synthesis of long single-walled carbon nanotube strands. *Science* **2002,** *296* (5569), 884-886.
11. Zhou, T.; Niu, Y. T.; Li, Z.; Li, H. F.; Yong, Z. Z.; Wu, K. J.; Zhang, Y. Y.; Li, Q. W., The synergetic relationship between the length and orientation of carbon nanotubes in direct spinning of high-strength carbon nanotube fibers. *Mater. Des.* **2021,** *203*, 109557.
12. Zhang, X.; De Volder, M.; Zhou, W. B.; Issman, L.; Wei, X. J.; Kaniyoor, A.; Portas, J. T.; Smail, F.; Wang, Z. B.; Wang, Y. C.; Liu, H. P.; Zhou, W. Y.; Elliott, J.; Xie, S. S.; Boies, A., Simultaneously enhanced tenacity, rupture work, and thermal conductivity of carbon nanotube fibers by raising effective tube portion. *Sci. Adv.* **2022,** *8* (50), eabq3515.
13. Cho, Y. S.; Lee, J. W.; Kim, J.; Jung, Y.; Yang, S. J.; Park, C. R., Superstrong carbon nanotube yarns by developing multiscale bundle structures on the direct spin-line without post-treatment. *Adv. Sci.* **2023,** *10* (2), 2204250.
14. Kinoshita, T.; Karita, M.; Chikyu, N.; Nakano, T.; Inoue, Y., Enhancement of catalytic activity by addition of chlorine in chemical vapor deposition growth of carbon nanotube forests. *Carbon* **2022,** *196*, 391-400.
15. Zhang, M.; Atkinson, K. R.; Baughman, R. H., Multifunctional carbon nanotube yarns by downsizing an ancient technology. *Science* **2004,** *306* (5700), 1358-1361.
16. Zhang, X. F.; Li, Q. W.; Holesinger, T. G.; Arendt, P. N.; Huang, J. Y.; Kirven, P. D.; Clapp, T. G.; DePaula, R. F.; Liao, X. Z.; Zhao, Y. H.; Zheng, L. X.; Peterson, D. E.; Zhu, Y. T., Ultrastrong, stiff, and lightweight carbon-nanotube fibers. *Adv. Mater.* **2007,** *19* (23), 4198-4201.
17. Jia, J. J.; Zhao, J. N.; Xu, G.; Di, J. T.; Yong, Z. Z.; Tao, Y. Y.; Fang, C. O.; Zhang, Z. G.; Zhang, X. H.; Zheng, L. X.; Li, Q. W., A comparison of the mechanical properties of fibers spun from different carbon nanotubes. *Carbon* **2011,** *49* (4), 1333-1339.
18. Zhang, X. F.; Li, Q. W.; Tu, Y.; Li, Y. A.; Coulter, J. Y.; Zheng, L. X.; Zhao, Y. H.; Jia, Q. X.; Peterson, D. E.; Zhu, Y. T., Strong carbon-nanotube fibers spun from long carbon-nanotube

arrays. *Small* **2007,** *3* (2), 244-248.
19. Liu, K.; Zhu, F.; Liu, L.; Sun, Y. H.; Fan, S. S.; Jiang, K. L., Fabrication and processing of high-strength densely packed carbon nanotube yarns without solution processes. *Nanoscale* **2012,** *4* (11), 3389-3393.
20. Miaudet, P.; Badaire, S.; Maugey, M.; Derre, A.; Pichot, V.; Launois, P.; Poulin, P.; Zakri, C., Hot-drawing of single and multiwall carbon nanotube fibers for high toughness and alignment. *Nano Lett.* **2005,** *5* (11), 2212-2215.
21. Taylor, L. W.; Dewey, O. S.; Headrick, R. J.; Komatsu, N.; Peraca, N. M.; Wehmeyer, G.; Kono, J.; Pasquali, M., Improved properties, increased production, and the path to broad adoption of carbon nanotube fibers. *Carbon* **2021,** *171*, 689-694.
22. Vigolo, B.; Penicaud, A.; Coulon, C.; Sauder, C.; Pailler, R.; Journet, C.; Bernier, P.; Poulin, P., Macroscopic fibers and ribbons of oriented carbon nanotubes. *Science* **2000,** *290* (5495), 1331-1334.
23. Tsentalovich, D. E.; Headrick, R. J.; Mirri, F.; Hao, J. L.; Behabtu, N.; Young, C. C.; Pasquali, M., Influence of carbon nanotube characteristics on macroscopic fiber properties. *ACS Appl. Mater. Interfaces* **2017,** *9* (41), 36189-36198.
24. Jiao, X. Y.; Shi, C.; Zhao, Y. M.; Xu, L. L.; Liu, S. K.; Hou, P. X.; Liu, C.; Cheng, H. M., Efficient fabrication of high-quality single-walled carbon nanotubes and their macroscopic conductive fibers. *ACS Nano* **2022,** *16* (12), 20263-20271.
25. Liu, Y. D.; Kumar, S., Recent progress in fabrication, structure, and properties of carbon fibers. *Polym. Rev.* **2012,** *52* (3-4), 234-258.
26. Zaleski, D. P.; Sivaramakrishnan, R.; Weller, H. R.; Seifert, N. A.; Bross, D. H.; Ruscic, B.; Moore, K. B.; Elliott, S. N.; Copan, A. V.; Harding, L. B.; Klippenstein, S. J.; Field, R. W.; Prozument, K., Substitution reactions in the pyrolysis of acetone revealed through a modeling, experiment, theory paradigm. *J. Am. Chem. Soc.* **2021,** *143* (8), 3124-3142.
27. Tong, T. Z.; Liu, W. M.; Yan, J.; Qian, L.; Zhang, J., Growth of high-density horizontal SWNT arrays by pre-cracking of carbon source. *Carbon* **2023,** *205*, 27-32.